

The Lyman Continuum Escape Fraction of Star-forming Galaxies at $2.4 \lesssim z \lesssim 3.7$ from UVCANDELS

XIN WANG,^{1,2,3} HARRY I. TEPLITZ,⁴ BRENT M. SMITH,⁵ ROGIER A. WINDHORST,⁵ MARC RAFELSKI,^{6,7} VIHANG MEHTA,⁴ ANAHITA ALAVI,⁴ GABRIEL BRAMMER,^{8,9} JAMES COLBERT,⁴ NORMAN GROGIN,⁶ NIMISH P. HATHI,⁶ ANTON M. KOEKEMOER,⁶ LAURA PRICHARD,⁶ CLAUDIA SCARLATA,¹⁰ BEN SUNNQUIST,⁶ PABLO ARRABAL HARO,¹¹ CHRISTOPHER CONSELICE,¹² ERIC GAWISER,¹³ YICHENG GUO,¹⁴ MATTHEW HAYES,¹⁵ ROLF A. JANSEN,⁵ ZHIYUAN JI,¹⁶ RAY A. LUCAS,⁶ ROBERT O'CONNELL,¹⁷ BRANT ROBERTSON,¹⁸ MICHAEL RUTKOWSKI,¹⁹ BRIAN SIANA,²⁰ EROS VANZELLA,²¹ TERESA ASHCRAFT,⁵ MICAELA BAGLEY,²² IVANO BARONCHELLI,^{23,24} GUILLERMO BARRO,²⁵ ALEX BLANCHE,⁵ ADAM BROUSSARD,¹³ TIMOTHY CARLETON,⁵ NIMA CHARTAB,²⁶ YINGJIE CHENG,²⁷ ALEX CODOREANU,²⁸ SETH COHEN,⁵ Y. SOPHIA DAI,²⁹ BEHNAM DARVISH,²⁰ ROMEEEL DAVÉ,³⁰ LAURA DEGROOT,³¹ DUILIA DE MELLO,³² MARK DICKINSON,¹¹ NAJMEH EMAMI,²⁰ HENRY FERGUSON,⁶ LEONARDO FERREIRA,³³ KEELY FINKELSTEIN,²² STEVEN FINKELSTEIN,²² JONATHAN P. GARDNER,³⁴ TIMOTHY GBUREK,²⁰ MAURO GIAVALISCO,¹⁶ ANDREA GRAZIAN,²³ CARYL GRONWALL,^{35,36} SHOUBANEH HEMMATI,⁴ JUSTIN HOWELL,⁴ KARTHEIK IYER,³⁷ SUGATA KAVIRAJ,³⁸ PETER KURCZYNSKI,³⁴ ILIN LAZAR,³⁹ JOHN MACKENY,⁶ KAMESWARA BHARADWAJ MANTHA,¹⁰ ALEC MARTIN,¹⁴ GARRETH MARTIN,^{40,41} TYLER MCCABE,⁵ BAHRAM MOBASHER,²⁰ KALINA NEDKOVA,⁷ CHARLOTTE OLSEN,¹³ LILLIAN OTTESON,⁵ SWARA RAVINDRANATH,⁶ CALEB REDSHAW,⁵ ZAHRA SATTARI,²⁰ EMMARIS SOTO,⁴² L. Y. AARON YUNG,³⁴ BONNABELLE ZABELLE,¹⁰ AND
THE UVCANDELS TEAM

¹School of Astronomy and Space Science, University of Chinese Academy of Sciences (UCAS), Beijing 100049, China

²Institute for Frontiers in Astronomy and Astrophysics, Beijing Normal University, Beijing 102206, China

³National Astronomical Observatories, Chinese Academy of Sciences, Beijing 100101, China

⁴IPAC, Mail Code 314-6, California Institute of Technology, 1200 E. California Blvd., Pasadena CA, 91125, USA

⁵School of Earth and Space Exploration, Arizona State University, Tempe, AZ 85287, USA

⁶Space Telescope Science Institute, Baltimore, MD 21218, USA

⁷Department of Physics and Astronomy, Johns Hopkins University, Baltimore, MD 21218, USA

⁸Cosmic Dawn Center (DAWN), Denmark

⁹Niels Bohr Institute, University of Copenhagen, Jagtvej 128, DK-2200 Copenhagen N, Denmark

¹⁰Minnesota Institute of Astrophysics and School of Physics and Astronomy, University of Minnesota, Minneapolis, MN 55455, USA

¹¹NSF's NOIRLab, Tucson, AZ 85719, USA

¹²School of Physics and Astronomy, The University of Nottingham, University Park, Nottingham NG7 2RD, UK

¹³Department of Physics and Astronomy, Rutgers, The State University of New Jersey, Piscataway, NJ 08854, USA

¹⁴Department of Physics and Astronomy, University of Missouri, Columbia, MO 65211, USA

¹⁵Stockholm University, Department of Astronomy and Oskar Klein Centre for Cosmoparticle Physics, AlbaNova University Centre, SE-10691, Stockholm, Sweden

¹⁶Department of Astronomy, University of Massachusetts, Amherst, MA 01003, USA

¹⁷Department of Astronomy, University of Virginia, Charlottesville, VA 22904

¹⁸Department of Astronomy and Astrophysics, University of California, Santa Cruz, Santa Cruz, CA 95064, USA

¹⁹Department of Physics and Astronomy, Minnesota State University Mankato, Mankato, MN 56001, USA

²⁰Department of Physics and Astronomy, University of California, Riverside, Riverside, CA 92521, USA

²¹INAF – OAS, Osservatorio di Astrofisica e Scienza dello Spazio di Bologna, via Gobetti 93/3, I-40129 Bologna, Italy

²²Department of Astronomy, The University of Texas at Austin, Austin, TX 78712, USA

²³INAF-Osservatorio Astronomico di Padova, Vicolo dell'Osservatorio 5, I-35122, Padova, Italy

²⁴Dipartimento di Fisica e Astronomia, Università di Padova, vicolo Osservatorio, 3, I-35122 Padova, Italy

²⁵Department of Physics, University of the Pacific, Stockton, CA 95211, USA

²⁶Observatories of the Carnegie Institution of Washington, Pasadena, CA 91101, US

²⁷Department of Astronomy, University of Massachusetts, Amherst, 01003 MA, USA

²⁸Centre for Astrophysics and Supercomputing, Swinburne University of Technology, Hawthorn VIC 3122, Australia

²⁹National Astronomical Observatories, Chinese Academy of Sciences, Chaoyang District Beijing 100012, China

³⁰Institute for Astronomy, University of Edinburgh, Edinburgh, EH9 3HJ, UK

³¹College of Wooster, Wooster, OH 44691, USA

³²Department of Physics, The Catholic University of America, Washington, DC 20064, USA

³³Centre for Astronomy and Particle Physics, School of Physics and Astronomy, University of Nottingham, NG7 2RD, UK

³⁴Astrophysics Science Division, NASA Goddard Space Flight Center, Greenbelt, MD 20771, USA

³⁵Department of Astronomy & Astrophysics, The Pennsylvania State University, University Park, PA 16802, USA

Corresponding author: Xin Wang

xwang@ucas.ac.cn

³⁶*Institute for Gravitation and the Cosmos, The Pennsylvania State University, University Park, PA 16802, USA*

³⁷*Dunlap Institute for Astronomy & Astrophysics, University of Toronto, 50 St George Street, Toronto, ON M5S 3H4, CA*

³⁸*Centre for Astrophysics Research, Department of Physics, Astronomy and Mathematics, University of Hertfordshire, Hatfield, AL10 9AB, UK*

³⁹*Department of Galaxies and Cosmology, Max Planck Institute for Astronomy, Königstuhl 17, 69117 Heidelberg*

⁴⁰*Korea Astronomy and Space Science Institute, Yuseong-gu, Daejeon 34055, Korea*

⁴¹*Steward Observatory, University of Arizona, Tucson, AZ 85719, USA*

⁴²*Computational Physics, Inc., Springfield, VA 22151, USA*

Abstract

The UltraViolet Imaging of the Cosmic Assembly Near-infrared Deep Extragalactic Legacy Survey Fields (*UVCANDELS*) survey is a Hubble Space Telescope (*HST*) Cycle-26 Treasury Program, allocated in total 164 orbits of primary Wide-Field Camera 3 (WFC3) Ultraviolet and VISible light (UVIS) F275W imaging with coordinated parallel Advanced Camera for Surveys (ACS) F435W imaging, on four of the five premier extragalactic survey fields: GOODS-N, GOODS-S, EGS, and COSMOS. We introduce this survey by presenting a thorough search for galaxies at $z \gtrsim 2.4$ that leak significant Lyman continuum (LyC) radiation, as well as a stringent constraint on the LyC escape fraction (f_{esc}) from stacking the UV images of a population of star-forming galaxies with secure redshifts. Our extensive search for LyC emission and stacking analysis benefit from the catalogs of high-quality spectroscopic redshifts compiled from archival ground-based data and *HST* slitless spectroscopy, carefully vetted by dedicated visual inspection efforts. We report a sample of five galaxies as individual LyC leaker candidates, showing $f_{\text{esc}}^{\text{rel}} \gtrsim 60\%$ estimated using detailed Monte Carlo (MC) analysis of intergalactic medium (IGM) attenuation. We develop a robust stacking method to apply to five samples of in total 85 non-detection galaxies in the redshift range of $z \in [2.4, 3.7]$. Most stacks give tight $2\text{-}\sigma$ upper limits below $f_{\text{esc}}^{\text{rel}} < 6\%$. A stack for a subset of 32 emission-line galaxies shows tentative LyC leakage detected at $2.9\text{-}\sigma$, indicating $f_{\text{esc}}^{\text{rel}} = 5.7\%$ at $z \sim 2.65$, supporting the key role of such galaxies in contributing to the cosmic reionization and maintaining the UV ionization background. These new F275W and F435W imaging mosaics from *UVCANDELS* have been made publicly available on the Barbara A. Mikulski Archive for Space Telescopes (MAST).

Keywords: dark ages, reionization, first stars — galaxies: evolution — galaxies: high-redshift — intergalactic medium — ultraviolet: galaxies

1. INTRODUCTION

Cosmic reionization is the last major phase transition of the Universe when its bulk properties are altered by galaxies (see e.g., Fan et al. 2006; Stark 2016). There has been increasing evidence that young massive stars collectively dominate over supermassive black holes in the early Universe in producing the LyC photons (with rest-frame wavelength $\lambda_{\text{rest}} < 912\text{\AA}$) that reionize the neutral IGM at $z \sim 6\text{--}9$ (Dayal et al. 2020). However the exact fraction of these LyC photons that evade photoelectric and dust absorption from their origin galaxy and escape into the IGM to ionize it — f_{esc} — remains elusive and controversial (Finkelstein et al. 2019; Naidu et al. 2020), making f_{esc} one of the greatest unknowns in reionization studies. Furthermore, the intervening IGM transmission drops precipitously at $z \geq 4$, due to the steeply rising IGM opacity, τ_{IGM} (Inoue et al. 2014). As a result, it is basically impractical to directly measure any LyC leakage in the epoch of reionization (EoR).

A more feasible way forward is thus to find low-redshift galaxies that are analogous to those $\gtrsim 13$ Gyrs ago, which

are thought to drive the reionization process. The constraints and measurements of their LyC f_{esc} and its correlation with their physical properties can help shed light upon the detailed physical mechanism conducive to the escape of the ionizing radiation into the IGM, surviving the absorption by the intervening H I gas and dust in the interstellar medium (ISM) or circumgalactic medium (CGM) (Steidel et al. 2018).

Due to the intrinsic faintness of LyC flux, the searches for LyC leakage at any cosmological distances have been very challenging. Generally speaking, currently available ultraviolet (UV) instrumentation leads to fruitful detection of LyC leakage at primarily two redshift windows. One is at $z \sim 0.3$, where LyC can be captured by the space-based far-UV spectroscopy (see e.g., Leitherer et al. 1995; Bergvall et al. 2006; Borthakur et al. 2014; Izotov et al. 2016, 2018). The recent *HST* Cosmic Origin Spectrograph (COS) campaigns have led to the detection of LyC signals in several dozen targets at $z \sim 0.3$, which are usually compact isolated galaxies with high ionization and extreme star formation, a.k.a. Green Peas (GPs) (see e.g., Izotov et al. 2021; Flury et al. 2022). Yet the

complex selection function and dissimilar environments of these $z \sim 0.3$ GPs make it difficult to generalize these findings to the EoR (Naidu et al. 2021).

The other major redshift range, much closer to the EoR in time, is at $z \sim 2-3$ where LyC flux is accessible to ground-based blue-sensitive instruments (see e.g., Marchi et al. 2018; Steidel et al. 2018; Pahl et al. 2021; Saxena et al. 2021) or *HST* WFC3 UVIS imaging (see e.g., Vanzella et al. 2016; Bian et al. 2017; Naidu et al. 2017; Fletcher et al. 2019; Rivera-Thorsen et al. 2019; Yuan et al. 2021; Prichard et al. 2022). These studies are progressively reaching a consensus in support of an intriguing bimodality of f_{esc} .

On one hand, there exists a population of sources with super- L_* UV luminosities that leak surprisingly large amount of ionizing radiation with $f_{\text{esc}} \gtrsim 50\%$, e.g., ION1 at $z = 3.8$ (Vanzella et al. 2012; Ji et al. 2020), ION2 at $z = 3.2$ (Barros et al. 2016; Vanzella et al. 2016), ION3 at $z = 4$ (Vanzella et al. 2018), the SUNBURST arc at $z = 2.37$ (Rivera-Thorsen et al. 2019), Q1549-C25 at $z = 3.2$ (Shapley et al. 2016), etc.. On the other hand, there are far more galaxies on which only upper limits can be derived, despite deep imaging and spectroscopy (tens of hours of integration on a 8/10-m diameter ground-based telescope or *HST*) (Malkan et al. 2003; Siana et al. 2007, 2010, 2015; Vasei et al. 2016; Alavi et al. 2020). Stacking these non-detections produces population-averaged f_{esc} with tight upper limits of 5-10% for $\gtrsim 0.5L_*$ galaxies at $z \sim 3$ (Rutkowski et al. 2017; Steidel et al. 2018; Begley et al. 2022).

At face value, this tight upper limit does not bode well for the completion of reionization by $z \sim 6$, which requires $f_{\text{esc}} \sim 10-20\%$ under the canonical reionization picture (Robertson et al. 2013, 2015). This crisis can be largely alleviated though, if one or several of the following conditions are met. 1) Galaxies produce and leak ionizing photons more efficiently at higher redshifts and lower stellar mass (Finkelstein et al. 2019). 2) Reionization is instead driven by a much rarer class of massive, bright galaxies ($M_{\text{UV}} \lesssim -20$ and $M_* \gtrsim 10^{8.5} M_\odot$) with much higher f_{esc} and ionizing photon production efficiency (the oligarch scenario, Naidu et al. 2020, 2021). 3) The completion of reionization is delayed to redshift of $z \sim 5$ (Kulkarni et al. 2019). Furthermore, f_{esc} is closely tied to other galaxy properties (stellar mass, star formation rate, stellar initial mass function, metallicity, etc.), while the overall emissivity caused by the entire galaxy population also depends on the shape and cutoff of the luminosity function.

The Ultraviolet Imaging of the Cosmic Assembly Near-infrared Deep Extragalactic Legacy Survey Fields (*UVCANDELS*) survey is a *HST* Cycle-26 Treasury Program (*HST*-GO-15647, PI: Teplitz), awarded a sum of 164 orbits of primary Wide Field Camera 3 (WFC3) UVIS/F275W imaging with coordinated parallel Advanced Camera for Survey

(ACS) F435W imaging, on four of the five premier extragalactic survey fields: GOODS-N, GOODS-S, EGS, and COSMOS. The *UVCANDELS* dataset is unique in further testing the LyC leakage bimodality mentioned above, since it is the uniform UV dataset surveying the largest area with UVIS, amounting to $\sim 426 \text{ arcmin}^2$, with extensive spectroscopic redshift measurements. The UV images across the entire fields, reaching a $5-\sigma$ sensitivity of $\text{mag}_{\text{F275W}}=27$ for compact sources, are taken at Hubble’s angular resolution. This is critical, since a key necessity in LyC searches is to confirm the origin of these faint signals with high spatial resolution imaging/spectroscopy, in order to exclude the possibility of foreground contamination from low- z interlopers along the line of sight (see e.g., Steidel et al. 2001; Iwata et al. 2009; Vanzella et al. 2010, 2012; Nestor et al. 2011, 2013; Mostardi et al. 2013).

This paper is organized as follows. In Sect. 2, we first present a comprehensive overview of the key science drivers of the *UVCANDELS* Treasury Program. In Sect. 3, we present the observing strategy and data reduction details. We then explain the selection of our galaxy sample with spectroscopic redshifts in Sect. 4. In Sect. 5, we describe our image stacking techniques and show the results. The inference of the LyC f_{esc} is given in Sect. 6. Finally, we conclude in Sect. 7. Throughout this paper, the standard AB magnitude system is used (Oke & Gunn 1983).

2. SCIENCE OVERVIEW OF *UVCANDELS*

UVCANDELS provides extensive UVIS imaging in four of the five premier *HST* deep-wide survey fields: GOODS-N, GOODS-S, EGS, and COSMOS, targeted by the Cosmic Assembly Near-infrared Deep Extragalactic Legacy Survey (*CANDELS*, Grogin et al. 2011; Koekemoer et al. 2011). *UVCANDELS* takes primary WFC3 F275W exposures at a uniform 3-orbit depth and coordinated parallel Advanced Camera for Survey (ACS) F435W exposures at slightly varying depth resulting from the roll angle constraints and the overlap from the increased FoV of the ACS camera. In total, the UV coverage secured by *UVCANDELS* reaches $\sim 426 \text{ arcmin}^2$ ¹, a factor of 2.7 larger than all previous data combined, including the WFC3 ERS UVIS imaging in GOODS-South (Windhorst et al. 2011), the *CANDELS* F275W Continuous Viewing Zone (CVZ) imaging in GOODS-North (Grogin et al. 2011), the UVUDF imaging in the Hubble Ultradeep Field within GOODS-South (Teplitz et al. 2013; Rafelski et al. 2015), and the HDUV covering portions of both GOODS fields (Oesch et al. 2018). This unique data set enables a wide range of scientific explorations as follows (Wang et al. 2020):

¹ The number of pointings in each *UVCANDELS* fields are 16 in GOODS-N, 8 in GOODS-S, 20 in EGS, and 16 in COSMOS.

- Using the high spatial resolution UV and Blue data (700 pc at $z \sim 1$) to study the structural evolution of galaxies and create 2D maps of their star-formation history;
- Combining *UVCANDELS* with the valuable Herschel legacy far-infrared data to trace the evolution of the star-formation, gas and dust content of moderate redshift ($z < 1$) galaxies;
- Probing the role of environment in the evolution of low-mass ($\lesssim 10^9 M_\odot$) star-forming galaxies at $z \sim 1$;
- Investigating the decay of star-formation in massive early type galaxies and the role of minor mergers since $z \sim 1.5$;
- Constraining the escape fraction of ionizing radiation (with $\lambda_{\text{rest}} \leq 912 \text{ \AA}$) from galaxies at $z \gtrsim 2.4$ to better understand how star-forming galaxies reionized the Universe at $z > 6$.

In addition, this unique *UVCANDELS* data set has additional treasury value: UV data break the degeneracy between the Balmer break and Lyman break spectral features (Rafelski et al. 2015) to improve the photo- z accuracy. HST UV data complement the existing and newly obtained ground-based U-band surveys in the *CANDELS* fields (Ashcraft et al. 2018; Redshaw et al. 2022).

3. OBSERVATIONS AND DATA REDUCTION

3.1. *UVCANDELS* observations

The *UVCANDELS* program (*HST*-GO-15647, PI: Teplitz) obtained F275W and F435W (coordinated parallel) imaging of four of the *CANDELS* fields (see Fig. 1, providing new UV (F275W) and wide-area blue optical (F435W) coverage in the COSMOS and EGS fields, and doubling the UV area in GOODS).

The survey was designed to reach a $5\text{-}\sigma$ limiting magnitude of $\text{mag}_{\text{F275W}}=27$ for compact galaxies (with $0''.2$ radius), which corresponds to an unobscured star-formation rate (SFR) limit of $0.2 M_\odot/\text{yr}$ at $z \sim 1$. This goal required about 8100 seconds per pointing in F275W (3 orbits of two ~ 1350 sec exposures each). A minimum of 6 exposures were required for good rejection of cosmic rays (CR), which was determined using the archival UVUDF Teplitz et al. (2013) dataset. As a result, *UVCANDELS* did not choose the full-orbit exposures that are optimized for deep surveys with greater on-sky redundancy. In GOODS-N, CVZ increased the efficiency of the observations.

Following the Space Telescope Science Institute’s best practices, exposures included post-flash to mitigate the effects of UVIS charge transfer efficiency (CTE) degradation (Mackenty & Smith 2012). Post-flash protects against the

loss of the faintest objects by filling “traps” on the charge-coupled devices (CCDs) before readout. The selected post-flash level brings the on-chip background up to $12 e^-$ per pixel on average.

The F435W parallels have varying depth due to the overlap from the increased field of view (FOV) of the ACS camera. In COSMOS and EGS, most of the area has 3 orbit depth with 5σ sensitivity of $\text{mag}_{\text{F435W}}=28$, while the overlap region have 6 orbit depth and a sensitivity of $\text{mag}_{\text{F435W}}=28.4$. The GOODS fields already have B-band coverage of sufficient coverage ($\text{mag}_{\text{F435W}} \sim 28$), so the additional F435W data were placed in the central *CANDELS*-Deep region, where deep archival UV and near-infrared (NIR) data are available.

UVCANDELS comprised 164 orbits of primary UVIS/F275W with ACS/F435W in parallel. Figure 1 show the *UVCANDELS* F275W and F435W footprints overlaid on the *CANDELS* optical imaging mosaics. Small gaps between individual exposures in the F435W coverage are not shown in the figures. The COSMOS and EGS were targeted for 16 and 20 pointings, respectively (approximately 2×8 and 2×10 , adjusted for scheduling flexibility), enabling F435W coverage in parallel over most of the UV area. In GOODS-S, *UVCANDELS* obtained 8 pointings, to complete coverage of the field. In GOODS-N, *UVCANDELS* observed two groups of 8 pointings (2×4), partially during CVZ and near-CVZ opportunities. The survey design employed a standard dithering pattern of WFC3-UVIS-DITHER-LINE to enable recovery of spatial resolution using *ASTRODRIZZLE* to create mosaics (see Sect. 3.2 for more details).

In most cases, each pointing was observed in a single visit to enable robust CR rejection. In a few cases, guide star limitations required splitting observations into 2-orbit and 1-orbit visits. In 3 visits, initial observations failed and re-observations were obtained. 1 visit in the EGS fields failed after more than 90% of the program had been completed, and so were not reobserved.

3.2. *HST* data reduction

The WFC3/UVIS and ACS/WFC images were calibrated using custom routines developed in Rafelski et al. (2015); Prichard et al. (2022), and specifically for the *UVCANDELS* data. In order to correct for radiation damage of the WFC3/UVIS detector over time, the F275W data were corrected with the updated charge transfer efficiency (CTE) correction algorithm (Anderson et al. 2021) which includes reduced noise amplification over previous efforts. These F275W images also include the official improved calibrations after 2021 that include concurrent dark subtraction to reduce the blotchy pattern otherwise observed in WFC3/UVIS images and updated flux calibration to match the latest CALSPEC models, which is especially important in the UV (Calamida et al. 2021). We generate custom hot pixel masks

using co-temporal darks and a variable threshold as a function of the distance to the readout to ensure a uniform number of hot pixels across the CCDs².

In addition, we flag readout cosmic rays (ROCRs) in the F275W data by identifying cosmic rays that fall on the detector after the readout of the amplifiers has begun, which are more apparent with the improved CTE correction code. The ROCRs appear as negative divots in the images due to over-correction by the CTE code, as the ROCRs land closer to the amplifiers than is recorded. The ROCRs are identified as 3 sigma negative outliers within 5 pixels of the readout direction of cosmic ray hits identified with AstroDrizzle. These negative pixels have the data quality flags set as bad pixels. Finally, we equalize the background levels on the four amplifiers as their bias level is likely affected by CTE degradation of the overscan regions. This results in clean images with constant background levels³.

We also correct for scattered light in the WFC/ACS F435W images likely caused by earth limb light reflected off the telescope structure (Biretta et al. 2003; Dulude et al. 2010). Each exposure is checked for the existence of a gradient by comparing the left quarter to the right quarter of the image, and a difference threshold of $5e^-$ is applied to a 3 sigma clipped median. If over the threshold, sources are masked in the image and the gradient is modeled with the PHOTUTILS Background2D module. Afterwards, the background level of the two chips is equalized to the mean level determined from a $3-\sigma$ clipped mean after source masking⁴.

3.3. Image mosaicing

The image registration and stacking pipeline was adapted from the one used in Alavi et al. (2014). Briefly, the calibrated, flat fielded WFC3/UVIS and ACS/WFC images were combined with the AstroDrizzle software package (Gonzaga 2012). To this end, first, we use the TWEAKREG task in the PYRAF/DRIZZLEPAC package to align the individual calibrated images within every single visit to ensure relative astrometric alignment. We then run the ASTRODRIZZLE pipeline on each visit and align the drizzled output image to the CANDELS astrometric reference grid to correct for the small offset in pointing and rotation from different visits with different guide stars. We performed the alignment on the 30 mas/pix images, with a precision of 0.15 pixel, using unsaturated stars and compact sources. These astrometric solutions are then transferred back to the header of the original calibrated flat fielded data using the TWEAKBACK task in the PYRAF/DRIZZLEPAC package. In the end, all of these aligned calibrated

Table 1. Values of some key ASTRODRIZZLE parameters set in creating the new F275W and F435W mosaics from UVCANDELS observations.

Parameter	Value
driz_cr_corr	True
driz_combine	True
clean	True
final_wcs	True
final_scale	0.06 (0.03)
final_pixfrac	0.8
final_kernel	square
skymethod	globalmin+match
skysub	True
combine_type	imedian

images are drizzled to the same pixel scale of 60 (30) milliarcsec matched to the CANDELS reference images for the various fields⁵. Table 1 provides the drizzle parameters that were used. The overall image footprints are shown in Fig. 1.

ASTRODRIZZLE removes the background, rejects cosmic rays, and corrects input images for geometric distortion. In addition to the science images, ASTRODRIZZLE generates an inverse variance map (IVM), which we use later to make weight images and to calculate photometry uncertainties. We apply the additional correction to the weight images to account for the correlated noise following Casertano et al. (2000). We make publicly available these image mosaics on MAST⁶.

4. SAMPLE SELECTIONS AND SPECTROSCOPIC REDSHIFTS

The focus of our LyC investigation is to measure or set strict limits on the escape fractions of LyC photons from galaxies at redshifts $z \gtrsim 2.4$. When the red end of the filter response is below the rest-frame Lyman limit, then detected signal can be interpreted as LyC emission (see e.g. Smith et al. 2018, 2020). For this technique to succeed, it is important that the study relies on secure galaxy redshifts. In this section, we discuss the sample selection that enables our search for LyC escape.

4.1. Redshift catalogs

To achieve precise, uncontaminated LyC flux measurements, we chose galaxies with high quality and accurate

² https://github.com/lprichard/HST_FLC_corrections

³ <https://github.com/bsunnquist/uvis-skydarks>

⁴ https://github.com/bsunnquist/uvis-skydarks/blob/master/remove_gradients.ipynb

⁵ <https://archive.stsci.edu/hlsp/candels>

⁶ <https://archive.stsci.edu/hlsp/uvcandels>

spectroscopic redshifts. To accomplish this, we vetted each spectrum in our spectroscopic sample by eye, then selected only the spectra with the highest score ranks by multiple spectroscopy experts on our team.

Our initial compilation of archival spectral dataset comprises the Keck observations conducted by Barger et al. (2008); Jones et al. (2018, 2021), the C3R2 survey (Masters et al. 2019), the COSMOS-Magellan active galactic nucleus (AGN) survey (Trump et al. 2009), the DEEP2 survey (Newman et al. 2013), the DEIMOS 10K survey (Hasinger et al. 2018), the GOODS VLT/FORS2 survey (Vanzella et al. 2007), the GOODS VLT/VIMOS survey (Popesso et al. 2009; Balestra et al. 2010), GMASS (Kurk et al. 2013), the MOSDEF survey (Kriek et al. 2015), the MUSE-Wide survey (Herenz et al. 2017), Reddy et al. (2006), Szokoly et al. (2004), TKRS/TKRS2 (Wirth et al. 2004, 2015), VANDELS (Pentericci et al. 2018), VIPERS (Garilli et al. 2014), VUDS (Le Fèvre et al. 2015), VVDS (Le Fèvre et al. 2005), and zCOSMOS (Lilly et al. 2007).

We also supplement this extensive redshift catalog with additional sources identified in a reanalysis of archival *HST* near-infrared grism spectroscopy in the *CANDELS* fields, acquired by primarily the 3D-*HST* survey (Brammer et al. 2012; Momcheva et al. 2016). This reanalysis is part of a novel initiative dubbed the Complete Hubble Archive for Galaxy Evolution (CHARGE, see e.g., Kokorev et al. 2022). The state-of-the-art GRIZLI software⁷ (Brammer & Matharu 2021) is utilized to conduct uniform reprocessing of all archival *HST* imaging and slitless spectroscopy in the areas of *CANDELS* fields contained within our *UVCANDELS* footprints.

Briefly, GRIZLI reduces the paired pre-imaging and grism exposures in five steps. A) Pre-processing the raw WFC3 imaging and grism exposures. This step includes flat fielding, relative/absolute astrometric alignment, variable/master sky background removal, satellite trail masking, etc. B) Iterative forward-modeling the full field-of-view (FoV) grism exposures at visit level. C) Obtaining best-fit grism redshift of sources through spectral template synthesis. D) Refining the full FoV grism models. E) Extracting the science-enabling products (e.g. 1D/2D grism spectra, emission line maps, etc.) for sources of interest. During step C), GRIZLI calculates a number of goodness-of-fit statistics for the redshift fitting procedure. As in Wang et al. (2022a,b), we compiled a list of galaxies with secure grism redshifts at $z_{\text{grism}} \gtrsim 2.4$, when all of the following goodness-of-fit criteria are satisfied: $\chi^2_{\text{reduced}} < 1.5 \wedge (\Delta z)_{\text{posterior}} / (1 + z_{\text{peak}}) < 0.005 \wedge \text{BIC} > 30$. Here χ^2_{reduced} is the reduced χ^2 , $(\Delta z)_{\text{posterior}}$ represents the 1- σ width of redshift posteriors, and BIC stands for the

Bayesian information criterion estimated from the template fitting procedure. This provides us additional high-quality grism redshifts that we combine with the previous redshift compilations for the subsequent visual inspection, to select the highest fidelity sample for our stacking analysis. In addition, this coherent reanalysis of all the available archival grism exposures covering the entire *UVCANDELS* fields provides comprehensive measurements of the nebular emission line properties of our sample galaxies, which help divide the full sample into subgroups (see Sect. 4.2).

4.2. Visual inspection and sample selection

For our visual inspection, we assigned each spectrum to be visually vetted by at least four reviewers randomly chosen from a group of 13 spectroscopy experts. Each reviewer gave a score to the claimed redshift from the survey catalog, with the following rubric, i.e., 0: reliable, 1: possibly correct, or 2: incorrect. This ranking takes into account the alignment of the observed spectral features to their expected position given the reported redshift in the spectrum, the amount of visible noise, the shape of each line or other spectral feature, the presence of unknown/unexpected spectral lines, the presence of neighbors in the corresponding multiband *HST* images, and the drop-out band from the *HST* images. After ranking was completed, we separated each spectrum into five redshift quality quintiles, based on their median and average scores, where the first quintile has median<1 and average<0.5, the second quintile has median<1 and average<1, the third quintile has median<2 and average<1.5, the fourth quintile has average<2 and median<2, and the last quintile has median=2 and average=2. As a consequence, our first redshift quality quintile has 39 galaxies, second has 59, third has 202, fourth has 19, and fifth has 271. Example figures of galaxies in each quintile are shown in the Appendix §A.

In our analysis, we will rely on the most secure redshifts, referring to those in the first, second and third redshift quality quintiles identified by our reviewers. We base our decision to include the third quintile on experience with the overall high quality of the spectra in *CANDELS*. In this paper, we focus on the search of the LyC signals from individual leakers and/or stacking analysis using the *UVCANDELS* WFC3/F275W imaging data. So we trim the high-quality redshift catalog by filtering out all spectra taken outside of the *UVCANDELS* footprints (we defer the analysis outside the *UVCANDELS* footprints but within other archival UV imaging to a later work). We identify and exclude potential AGN candidates from the deep Chandra X-ray observations in these *CANDELS* fields (Hsu et al. 2014; Nandra et al. 2015; Xue et al. 2016, , and D. Kocevski priv. comm.), as we present the stacking analysis of the escaping LyC signals from AGNs in a companion work (Smith et al. 2023, in prep.). We also exclude sources that lie in close proximity to

⁷ <https://github.com/gbrammer/grizli>

detector chip gaps of the UVCANDELS F275W imaging, for complex noise properties due to insufficient dithering.

In the end, we compiled a list of 90 galaxies with high-quality spectroscopic redshifts in the range of $z \in [2.4, 3.7]$, based on our dedicated visual inspections of these publicly available spectra. Among these 90 galaxies, 5 show significant detection of their F275W fluxes with signal-to-noise ratio (SNR) ≥ 3 , which, combined with their secure redshift information, classify them as candidates of individual LyC leaking galaxies. We present the measurements of their detailed properties in Sect. 5.1. Aside from the 5 F275W detections, all the rest of 85 galaxies in our high-quality spectroscopic redshift sample show non-detections in F275W, and are analyzed in our stacking analysis elaborated in Sect. 5.2.

We define five sub-groups on which the stacking analysis is performed separately, for the purpose of testing the possible correlation between LyC leakage and galaxy global properties. To take into account the rapidly evolving IGM opacity with respect to redshift, we divide the entire 85 galaxies into three redshift samples: LOW- z bin ($z \in [2.4, 2.5]$), INTERMEDIATE- z bin ($z \in [2.5, 3.0]$), and HIGH- z bin ($z \in [3.0, 3.7]$). Galaxies in the LOW- z bin have their Lyman limit lying closer to the red edge of F275W than sources in the other two redshift bins. Then we classify all the galaxies in the first and second redshift quality quintiles with median score < 1 and average score < 1 (i.e. at least 3 out of 5 inspectors deem this redshift measurement secure) as the GOLD- z subsample. Last but not the least, we refer to the galaxies showing significant detection of [O II] $\lambda 3727, 3730$ (hereafter referred to as [O II]) emission in their WFC3/G141 grism spectra as the strong line emitter subsample, denoted by STRONG-[O II]. The total and break-down of the number counts for these stacking samples in individual fields are presented in Table 2.

5. IMAGE STACKING AND PHOTOMETRY

In this section, we first introduce some tentative detections of individual LyC leaker candidates probed by our modestly deep F275W imaging (in Sect. 5.1). Then we describe in detail our methodology of image stacking in Sect. 5.2, and aperture photometry of the stacked images in Sect. 5.3.

5.1. Potential individual LyC leaker candidates

Here, we identify 5 LyC leaker candidates, whose coordinates, redshifts, and photometry are presented in Table 3. These candidates all have secure spectroscopic redshifts vetted by our visual inspection efforts, and show significant F275W flux detected at $\text{SNR} \geq 3$.

Here we conduct UV-optimized aperture photometry on the new WFC3/F275W and ACS/F435W UVCANDELS data,

following the methodology developed as part of the Hubble Ultra-Deep Field UV analysis (Teplitz et al. 2013; Rafelski et al. 2015). This method regards the object optical isophotes as more appropriate apertures for counting UV photons than the isophotes defined in near-infrared wavelengths. The PSF and aperture corrections are then performed to make sure the UV and B-band fluxes are consistent with the previous measurements at other wavelengths. The detailed description of our UV-optimized aperture photometry method is described in Sun et al. *in prep.*

We perform detailed Bayesian inference of their stellar population properties, using the CIGALE software (Boquien et al. 2019) to fit their multi-wavelength photometric measurements, the majority of which are taken from the public CANDELS photometric catalogs, as published in Barro et al. (2019) and (Stefanon et al. 2017a) for GOODS-N and EGS, respectively.

We model the galaxy star-formation history (SFH) using the delayed τ model via the SFHDELAYED module, since the sudden onset of star formation and burst episodes in a, e.g., double-exponential parameterization (i.e. the SFH2EXP module) may be too abrupt when the variation of the SFH may be smoother (Boquien et al. 2019; Carnall et al. 2019). We also verify that the different choices of SFH models have a marginal effect on the estimated f_{esc} values, on average by $\sim 4\%$. We rely on the BC03 stellar population synthesis models (the bc03 module, Bruzual & Charlot 2003), the infrared dust models of Dale et al. (2014), and the Calzetti et al. (2000) dust extinction law, during the spectral energy distribution (SED) fitting with CIGALE. The resulting constraints of their SED properties are given in Table 3. In particular, we utilize the NEBULAR module and keep the parameter NEBULAR.F_ESC freely varying to allow for emission lines in the SED which were observed in their spectra.

To compute ‘‘intrinsic’’ LyC model flux for these sources (see Table 3), we calculate the inner product of the F275W filter throughput and the CIGALE SED using only the stellar (old and young), nebular lines and continuum (old and young), and dust emission components. The value of f_{esc} is simply the ratio of the observed flux in the UVCANDELS WFC3/UVIS F275W image to this modeled LyC flux in F275W, corrected for IGM attenuation. To perform this correction to the modeled LyC flux, we use the MC line-of-sight IGM attenuation code of (Inoue et al. 2014). Each f_{esc} value uses 10,000 simulated sight lines at the redshift of each galaxy. The particular line-of-sight IGM attenuation towards each galaxy is unknown, though it is constrained by the observed LyC flux in F275W and the modeled intrinsic F275W flux. For realizations of sight lines that resulted in $f_{\text{esc}} > 100\%$, we redraw a new IGM attenuation line-of-sight since these can not be in the set of possible attenuation sight lines based on the spatial and density distributions of IGM

Table 2. Number of sources with high-quality spectroscopic redshifts at $z \in [2.4, 3.7]$, compiled from publicly available archival spectroscopic observations. Among these 90 galaxies, 5 show modestly bright F275W flux at $\text{SNR} \geq 3$ as tentative LyC leakage signals (see Sect. 5.1), whereas the rest 85 galaxies show non-detections in the *UVCANDELS* F275W imaging data. These 85 galaxies are further separated into five samples for our stacking analysis (see Sect. 5.2).

	individual leaker candidate	stacking sample				
		LOW- z^a	INTERMEDIATE- z^a	HIGH- z^a	GOLD- z^b	STRONG-[O II] ^c
GOODS-N	4	12	10	7	10	13
GOODS-S	0	1	3	3	0	3
EGS	1	6	8	2	8	10
COSMOS	0	9	7	17	8	6
Combined	5	28	28	29	26	32

^aThe LOW- z , INTERMEDIATE- z , and HIGH- z samples refer to galaxies in the redshift range of $[2.4, 2.5]$, $[2.5, 3.0]$, and $[3.0, 3.7]$, with a median redshift of $z_{\text{median}} \sim 2.45$, $z_{\text{median}} \sim 2.75$, and $z_{\text{median}} \sim 3.3$, respectively.

^bThe GOLD- z sample includes galaxies with the most secure spectroscopic redshifts, compiled from our visual inspection efforts.

^cThe STRONG-[O II] sample showing significant [O II] emission with $\text{SNR}_{[\text{O II}]} \geq 3$, measured from their archival G141 spectra. These galaxies are considered to be prominent line emitters, highly likely those leaking copious amount of LyC flux.

absorbers used in the Inoue et al. (2014) code. Galaxies IDs 6226, 20748, and 22588 have approximately 11%, 29%, and 1% of the total IGM transmission sight-lines result in physical f_{esc} values, respectively. We tabulate the results of the MC f_{esc} analysis in Table 3 with $1-\sigma$ uncertainties.

Among these five likely candidates of LyC leaking galaxies, the most promising source is ID 6226 at $z = 3.23$ in the GOODS-N field, as shown in Fig. 2. Since GOODS-N is one of the most extensively studied extragalactic fields, there exists a wealth of imaging and spectroscopic data. In particular, the entire field is covered by the deep Keck/*MOSFIRE* infrared spectroscopy (2 hrs each in H and K bands) acquired by the MOSDEF program (Kriek et al. 2015). Furthermore, in the whole field there also exists *HST* grism spectroscopy of both G102 (2 orbits by *HST*-GO-13420, PI: Barro) and G141 (2 orbits by *HST*-GO-11600, PI: Weiner). From these existing deep *MOSFIRE* H- and K-band spectroscopy, we see pronounced nebular emission features of [O III], H β , and [O II] lines, with fluxes being 20.7 ± 0.3 , 5.4 ± 0.7 , and 9.8 ± 0.6 in units of $10^{-17} \text{ erg s}^{-1} \text{ cm}^{-2}$, respectively. The [O II] and Mg II lines are also clearly detected in *HST* grism spectroscopy. The wide wavelength coverage (0.8-1.7 μm) of this joint G102-G141 spectroscopy at Hubble’s angular resolution basically rules out any possibilities of foreground contamination, since only the spectral features at $z = 3.23$ are seen. ID06226’s F275W magnitude is 25.5 ABmag de-

tected at a $5-\sigma$ significance, indicating $f_{\text{esc}} \approx 60\%$ from our SED fitting analysis combined with our MC IGM attenuation corrections. In addition, the ground-based U-band imaging from both KPNO and LBC also independently confirm its LyC leakage (Ashcraft et al. 2018). The spectra, *HST* image stamps, and SED fitting results of the rest four LyC leaker candidates are shown in the Appendix §B.

5.2. Stacking methodology

Unlike the 5 galaxies presented above, the vast majority of our sample galaxies with secure spectroscopic redshifts only show non-detections (i.e. $\text{SNR} < 3$) in *UVCANDELS* F275W imaging data, with . Following similar SED fitting analyses outlined in Sect. 5.1, we derive the estimates of their absolute UV magnitudes (M_{UV}) and dust attenuation values (E(B-V)) shown as the histograms in Fig. 3.

As shown in Table 2, we further separate these 85 galaxies into five individual samples, to constrain the LyC escape fraction on a population level, taking into account the rapidly evolving LyC opacity in the IGM (Steidel et al. 2018; Bassett et al. 2021). We do not opt to include the 5 detections to avoid stacks dominated and biased by a few sources which can likely be extreme outliers. We adopt the following image stacking procedures, similar to those utilized in Smith et al. (2018); Alavi et al. (2020); Smith et al. (2020).

Table 3. Properties of galaxies showing relatively high WFC3/F275W flux ($\text{SNR} \geq 3$) as tentative LyC leakage signals. They all have secure spectroscopic redshifts at $z \geq 2.4$ confirmed by ground-based and/or *HST* grism spectroscopy, indicating that these F275W fluxes probe their escaping LyC radiation.

Field	ID	R.A. [deg.]	Decl. [deg.]	z_{spec}	Ref. ^a	HST photometry [ABmag]								Best-fit properties from CIGALE			
						F275W	$\text{SNR}_{\text{F275W}}$	F435W	F606W	F814W	F125W	F160W	$\log(M_*/M_\odot)$	SFR [M_\odot/yr]	E(B-V)	$\text{F275W}_{\text{int}}^b$	$f_{\text{esc}}^{\text{rel}b}$
GOODS-N	00453	189.159046	62.115474	3.656	1	26.58	3.0	26.13	24.28	23.98	24.09	23.92	10.40	24.29	0.09	27.1	...
GOODS-N	06226	189.179527	62.185702	3.231	1,2,3	25.49	5.0	24.52	23.38	23.00	22.70	22.32	11.21	279.37	0.18	27.1	$0.59^{+0.32}_{-0.12}$
GOODS-N	20748	189.378395	62.281930	2.504	3,4	26.35	3.4	25.30	24.61	24.53	23.88	23.44	10.14	24.37	0.18	24.1	$0.84^{+0.26}_{-0.26}$
GOODS-N	22588	189.311919	62.296512	2.486	1,4	25.63	7.2	24.70	24.23	24.17	24.08	24.10	9.09	37.22	0.09	25.7	> 0.86
EGS	21708	215.040642	52.995283	2.408	3	26.51	3.1	25.60	24.97	24.82	24.31	24.05	9.82	9.30	0.09	25.6	...

^a The references where these spectroscopic redshifts are sourced from. 1: Barger et al. (2008). 2: CHARGE (Kokorev et al. 2022). 3: MOSDEF (Kriek et al. 2015). 4: Reddy et al. (2006).

^b We perform detailed Bayesian inference of stellar population parameters via the CIGALE software (Boquien et al. 2019), using galaxies' multi-band photometry excluding their F275W flux, to produce the model-independent intrinsic F275W flux ($\text{F275W}_{\text{int}}$) used in the LyC escape fraction calculation. Here $f_{\text{esc}}^{\text{rel}}$ is the LyC relative escape fraction calculated from $\text{F275W}_{\text{int}}$ corrected for the IGM absorption using the Inoue et al. (2014) Monte Carlo IGM transmission code. Object ID = 22588 had a $f_{\text{esc}}^{\text{rel}} \sim 1$ so we only show the 1- σ lower limit. Two of our sources (ID = 453 and 21708) show unphysical $f_{\text{esc}}^{\text{rel}}$ values ($> 100\%$), and are still included here nonetheless for a complete analysis.

Consistent with the previous studies of LyC leakage that employ stacking procedures, we assume the galaxies selected in our sample to be self-similar, thus allowing us to stack them to make a more accurate measurement of the faint LyC flux.

1. We first make large cutout image stamps in multiple filters (F275W and F435W from our work described in Sect. 3.3, F606W and F814W from CANDELS) with size $10'' \times 10''$ on $0.''03$ plate scale, centered on each galaxy with secure spectroscopic redshift that passes our visual vetting described in 4.2. We choose the coadded mosaics on $0.''03$ plate scale to take full advantage of the high resolution of *HST* imaging. Yet note that at this stage the object coordinates (RA and Dec) are taken from the CANDELS/UVCANDELS multi-wavelength photometric catalogs that use H_{160} -band mosaics as the detection image (Guo et al. 2013; Nayyeri et al. 2017; Stefanon et al. 2017b; Barro et al. 2019). The light centroids measured in F160W and optical/UV filters often do not align, as they probe the rest-frame optical and UV wavelength ranges of our sources of interest.
2. To properly re-centroid the optical/UV image cutouts before stacking and at the same time mask possible neighboring contaminants, we utilize the PHOTUTILS software to perform photometry on these cutout images. We produce the white light image from the image cutouts in all available filters weighted by filter mean flux density (i.e. f_v , the PHOTFNU keyword), which is taken as the detection image. We mask regions of pixels in the image cutouts according to existing object isophotes already defined in the H_{160} -band segmentation maps from the CANDELS photometry.

3. After obtaining the segmentation map from the detection white light image cutout, we measure the isophotal fluxes associated with each of the segmentation regions in the individual filter image cutouts using PHOTUTILS, and select the region that has the brightest F606W flux, under the assumption that the ionizing radiation emerges from the areas dominated by the emission from young massive stars. This is critical in pinpointing the centroid of our galaxies' rest-frame UV light, where the LyC signal most likely originates.
4. We then make small cutout image stamps with $5'' \times 5''$, appropriately centered on the object's peak V_{606} -band flux (corresponding to object's UV-light-weighted centroid), with all contaminants masked. Fig. 4 demonstrates the entire procedures for our re-centroiding and masking strategy. We also estimate the local sky background and remove that from the SCI extension before stacking. We exclude all surrounding objects outside a certain circular aperture of 0.5 arcsec.
5. We adopt two numerical recipes to combine the surface brightness signals from small cutout image stamps of individual objects in terms of different weighting schemes: uniform weighting and UV luminosity weighting. The uniform weighting scheme can be described by

$$\bar{f} = \frac{\sum f_i}{N_{\text{obj}}}, \quad \sigma^2 = \frac{\sum \sigma_i^2}{N_{\text{obj}}^2}, \quad (1)$$

where f_i and σ_i stand for the flux and uncertainty of the i^{th} source among the entire number of N_{obj} that contribute to the stacks. \bar{f} and σ thus denote the stacked flux and uncertainty.

The UV luminosity (L_{UV}) weighting scheme is instead depicted by

$$\bar{f} = \frac{\Sigma(f_i/L_{UV}^i)}{N_{obj}} \cdot L_{UV}^{\text{median}}, \quad \sigma^2 = \frac{\Sigma(\sigma_i/L_{UV}^i)^2}{N_{obj}^2} \cdot (L_{UV}^{\text{median}})^2, \quad (2)$$

where L_{UV}^i represents the galaxy rest-frame UV luminosity converted from M_{UV} shown in Fig. 3. The uniform weighting equalizes contribution from every line of sight to the stack, such that a mean IGM correction is applicable. The L_{UV} weighting normalizes galaxy multi-band photometry before stacking as the LyC escape fraction is a relative quantity (Marchi et al. 2017; Steidel et al. 2018). In Sect. 6, we show results obtained from both stacking methods.

- Finally, we apply both weighting methods to the all galaxy samples listed in Table 2. The large spatial coverage of the *UVCANDELS* survey presents us an ideal opportunity of testing the strengths of escaping LyC signals as a function of galaxy global properties with sufficient sample statistics. The stacked images in multiple filters for the *STRONG-[O II]* galaxy sample consisting of 32 sources are presented in Fig. 5.

5.3. Photometry on image stacks

Before image stacking detailed in Sect. 5.2, we have already subtracted a constant from each cutout image stamp in each filter (F275W, F435W, F606W, and F814W) of each galaxy selected for stacking, to ensure that the mode of the local sky background of each galaxy is achromatically as close to zero as possible. Just in case there still remains some residual sky background signals that survive our stacking procedures, we perform another round of background estimation and removal before the photometry of stacked images. We apply a circular mask with a radius of 45 pixels (i.e. $1''.35$) to the central regions of the stacked images in each filter, and bin the unmasked background pixels according to the Freedman-Diaconis rule, following Smith et al. (2018, 2020). Then we derive the mode value of the resultant count-rate histogram of these surrounding pixels outside the central masked regions, as the remaining sky background in the stacked images. After subtracting off this remaining background, we make sure that the empty regions of our stacked images only contain random noise.

The sample median redshifts are given in Table 4. At these redshifts, the broad-band filters F435W and F606W probe the blue and red side of the rest-frame 1500 Å wavelength regime of source spectrum, conventionally regarded as the UV continuum (UVC). The escaping LyC signals are believed to originate from young star clusters comprising hot, massive O-type stars, which also dominate the

blue-UV wavelength range of the host galaxy's SED (see e.g., Vanzella et al. 2022). We therefore take the stacked F606W image as the detection image to derive the Kron elliptical aperture for flux measurements as shown in Fig. 5, to avoid diluting the SNRs of potential LyC signals inside unnecessarily large apertures enclosing mostly noise. Following the practice presented in Sect. 5.2, we utilize the *PHOTUTILS* software to measure the Kron auto fluxes in the stacked images in all four filters: F275W, F435W, F606W, and F814W. We adopt the following parameters for *PHOTUTILS*: `detect_thresh=5`, `analysis_thresh=5`, `detect_minarea=8`, `deblend_nthresh=32`, `deblend_mincont=0.001`. Finally, using the up-to-date zero points of all four filters, we convert these measured fluxes into total magnitudes given in Table 4. After averaging the best-fit *CIGALE* SEDs as discussed above, we find an insignificant red-leak of flux into the F275W filter redward of the 912Å Lyman break of $\sim 0.8\%$.

6. INFERENCE OF THE LYC ESCAPE FRACTION

In this section, we present the main results from our detailed stacking analysis. Following the standard nomenclature (e.g., Steidel et al. 2001; Siana et al. 2010, 2015; Steidel et al. 2018), we define the *relative* escape fraction of LyC as

$$f_{\text{esc}}^{\text{rel}} = \frac{(F_{\text{UVC}}/F_{\text{LyC}})_{\text{int}}}{(F_{\text{UVC}}/F_{\text{LyC}})_{\text{obs}}} \cdot \exp(\tau_{\text{IGM}}), \quad (3)$$

where $(F_{\text{UVC}}/F_{\text{LyC}})_{\text{int}}$ and $(F_{\text{UVC}}/F_{\text{LyC}})_{\text{obs}}$ represent the intrinsic and the observed ratios of the UVC and LyC fluxes, respectively, and τ_{IGM} is the IGM opacity. The transmission of the ionizing flux through the intervening IGM (i.e. $t_{\text{IGM}} = \exp(-\tau_{\text{IGM}})$) is a highly stochastic process, ascribed to its bimodal probability distribution function (PDF). Bassett et al. (2021) showed that the PDF of t_{IGM} can be depicted by a sudden rise towards $t_{\text{IGM}} \sim 0$ and a much less prominent second peak at higher values. Due to the strong degeneracy between f_{esc} and t_{IGM} , the inferred values of f_{esc} are often overestimated from the observations of galaxies leaking strong LyC flux under the assumption of a mean t_{IGM} , a.k.a. the IGM transmission bias. Fortunately, Bassett et al. (2021) verified that this bias is less fatal for large galaxy ensembles including LyC non-detections.

To determine the appropriate average IGM transmission value for each stack, we use the Inoue et al. (2014) MC code to generate 10,000 realizations of the line-of-sight IGM transmission models as a function of observed wavelength per galaxy at its known redshift. We then calculate the filter

Table 4. Measured photometry and physical properties of the selected galaxy samples from our stacking analyses using uniform weighting.

sample	N_{gal}	z_{median}^a	Aperture photometry on the stacked images ^b					Measured physical properties							
			mag _{F275W}	SNR _{F275W}	mag _{F435W}	mag _{F606W}	mag _{F814W}	M_{UV}	E(B-V)	$\left(\frac{F_{\text{UVC}}}{F_{\text{LyC}}}\right)_{\text{obs}}$	c, d	$\left(\frac{F_{\text{UVC}}}{F_{\text{LyC}}}\right)_{\text{int}}$	e	$\langle \bar{\tau}_{\text{IGM}} \rangle^f$	$f_{\text{esc}}^{\text{rel}} C$ [%]
LOW- z	28	2.45	29.38	<2.0	25.64	25.07	24.86	-20.41	0.21	>53.30		8.56	0.38	<6.1	<0.8
INTERMEDIATE- z	28	2.75	28.96	2.9	26.05	25.31	25.11	-20.52	0.15	28.78 [26.21, 32.13]		14.36	0.21	10.4 [9.2, 11.3]	2.4 [2.1, 2.6]
HIGH- z	29	3.30	29.52	<2.0	27.03	25.96	25.50	-20.68	0.17	>26.51		11.57	0.06	<2.6	<0.5
GOLD- z	26	2.57	29.35	<2.0	25.68	25.01	24.84	-20.60	0.18	>54.15		10.75	0.25	<4.9	<0.9
STRONG-[O II]	32	2.65	29.07	2.9	25.69	25.00	24.82	-20.65	0.18	42.57 [39.21, 47.62]		10.18	0.24	5.7 [5.1, 6.2]	1.0 [0.9, 1.1]

^a Sample median redshift.

^b Total magnitude and significance measured from the aperture photometry performed on stacked image stamps. For measurements under $2\text{-}\sigma$ significance, we provide their $2\text{-}\sigma$ limits.

^c For tentative detections with $\text{SNR} \geq 2$, the values reported here correspond to the direct measurements obtained from the respective stacks, followed by the bootstrapped $1\text{-}\sigma$ uncertainty ranges. For non-detections, we show the inferred $2\text{-}\sigma$ limits of these physical quantities.

^d The observed ratio of the UVC and the escaping LyC flux, converted from the photometry of the stacked F606W and F275W images.

^e The intrinsic ratio of the UVC and LyC flux. We compute this ratio for each galaxy within the stacking samples based on their best-fit intrinsic SED and take the median of the distribution as the intrinsic ratio for stacks, listed here.

^f The average IGM transmission for each stack, estimated using galaxies' best-fit intrinsic SED and the Inoue et al. (2014) Monte Carlo line-of-sight IGM code.

^g The relation between the absolute and relative escape fractions is given by $f_{\text{esc}}^{\text{abs}} = f_{\text{esc}}^{\text{rel}} 10^{-0.4 A_{\text{UV}}}$, where $A_{\text{UV}} = 10.33 E(B - V)$ is the Calzetti et al. (2000) dust reddening law.

Table 5. Measured photometry and physical properties of the selected galaxy samples from our stacking analyses using L_{UV} weighting.

sample	N_{gal}	z_{median}^a	Aperture photometry on the stacked images ^b					Measured physical properties							
			mag _{F275W}	SNR _{F275W}	mag _{F435W}	mag _{F606W}	mag _{F814W}	M_{UV}	E(B-V)	$\left(\frac{F_{\text{UVC}}}{F_{\text{LyC}}}\right)_{\text{obs}}$	c, d	$\left(\frac{F_{\text{UVC}}}{F_{\text{LyC}}}\right)_{\text{int}}$	e	$\langle \bar{\tau}_{\text{IGM}} \rangle^f$	$f_{\text{esc}}^{\text{rel}} C$ [%]
LOW- z	28	2.45	28.64	<2.0	25.83	25.10	24.81	-20.41	0.21	>26.07		8.56	0.38	<12.4	<1.7
INTERMEDIATE- z	28	2.75	28.60	2.9	26.18	25.41	25.15	-20.52	0.15	18.73 [17.10, 21.00]		14.36	0.21	15.9 [14.2, 17.4]	3.7 [3.2, 4.0]
HIGH- z	29	3.30	29.36	<2.0	27.03	26.08	25.60	-20.68	0.17	>20.52		11.57	0.06	<3.3	<0.6
GOLD- z	26	2.57	29.25	<2.0	25.81	25.16	24.94	-20.60	0.18	>43.35		10.75	0.25	<6.1	<1.1
STRONG-[O II]	32	2.65	28.82	2.9	25.80	25.10	24.93	-20.65	0.18	30.77 [28.87, 33.74]		10.18	0.24	8.0 [7.2, 8.4]	1.4 [1.3, 1.5]

^a Sample median redshift.

^b Total magnitude and significance measured from the aperture photometry performed on stacked image stamps. For measurements under $2\text{-}\sigma$ significance, we provide their $2\text{-}\sigma$ limits.

^c For tentative detections with $\text{SNR} \geq 2$, the values reported here correspond to the direct measurements obtained from the respective stacks, followed by the bootstrapped $1\text{-}\sigma$ uncertainty ranges. For non-detections, we show the inferred $2\text{-}\sigma$ limits of these physical quantities.

^d The observed ratio of the UVC and the escaping LyC flux, converted from the photometry of the stacked F606W and F275W images.

^e The intrinsic ratio of the UVC and LyC flux. We compute this ratio for each galaxy within the stacking samples based on their best-fit intrinsic SED and take the median of the distribution as the intrinsic ratio for stacks, listed here.

^f The average IGM transmission for each stack, estimated using galaxies' best-fit intrinsic SED and the Inoue et al. (2014) Monte Carlo line-of-sight IGM code.

^g The relation between the absolute and relative escape fractions is given by $f_{\text{esc}}^{\text{abs}} = f_{\text{esc}}^{\text{rel}} 10^{-0.4 A_{\text{UV}}}$, where $A_{\text{UV}} = 10.33 E(B - V)$ is the Calzetti et al. (2000) dust reddening law.

throughput weighted average of these transmission models for each line-of-sight using

$$\bar{t}_{\text{IGM}} = \frac{\int \exp(-\tau_{\text{IGM}}) \frac{T_{\text{F275W}}}{\lambda} d\lambda}{\int \frac{T_{\text{F275W}}}{\lambda} d\lambda} \quad (4)$$

with T_{F275W} representing the F275W filter throughput. This ensures that only the observed wavelengths within the F275W filter are considered in the IGM transmission calculations, and any wavelengths outside of the filter would not be used to calculate the average f_{esc} of the stack. The result is 85 sets of distributions of 10,000 IGM transmission values through the F275W filter, for the 85 galaxies in the entire redshift range. To estimate the appropriate IGM transmission values for the five stacks, we take the arithmetic mean of the IGM transmission distributions for galaxies that reside in the stacking samples, hereafter denoted as $\langle \bar{t}_{\text{IGM}} \rangle$. We rely on $\langle \bar{t}_{\text{IGM}} \rangle$ to break the degeneracy between t_{IGM} and f_{esc} , since $\langle \bar{t}_{\text{IGM}} \rangle$ is based on the MC approach, adequate for our large galaxy samples selected from a wide sky coverage of 426 arcmin² in total. The values of $\langle \bar{t}_{\text{IGM}} \rangle$ are given in Tables 4 and 5.

To obtain the appropriate values of the intrinsic flux ratio of UVC to LyC, we run extensive sets of CIGALE SED fitting analysis of all galaxies within the entire stacking samples, following the numerical setup described in Sect. 5.1. We again do not use the observed F275W flux to retrieve model independent intrinsic SED at the LyC wavelengths of all galaxies, adding together the various components (i.e. stellar, nebular lines and continuum, and dust) without IGM and ISM absorption. We then compute the inner products of this intrinsic SED and the filter throughput of F275W and F606W, covering the rest-frame LyC and 1,500 Å UVC, respectively, to estimate the intrinsic flux of LyC and UVC for each galaxy in the stacking samples. Finally, we take a median of all the intrinsic UVC to LyC flux ratios of galaxies that reside in each one of the stacks as the sample average $\left(\frac{F_{\text{UVC}}}{F_{\text{LyC}}}\right)_{\text{int}}$, shown in Tables 4 and 5. We note that these intrinsic ratios are consistent with the conventional values quoted in the literature, (e.g. Guaita et al. 2017; Rutkowski et al. 2017; Smith et al. 2018; Alavi et al. 2020).

Then the relative and absolute LyC escape fractions are connected via

$$f_{\text{esc}}^{\text{abs}} = f_{\text{esc}}^{\text{rel}} 10^{-0.4A_{\text{UV}}}, \quad (5)$$

where $A_{\text{UV}} = 10.33 E(B - V)$ following the Calzetti dust attenuation law (Calzetti et al. 2000) appropriate for high- z star-forming galaxies. We take the sample median value of $E(B - V)$ as the default dust extinction estimates when computing $f_{\text{esc}}^{\text{abs}}$. We adopt two stacking methodologies, i.e., the uniform and L_{UV} weighting schemes, and summarize all the measured physical properties for our stacking galaxy samples

in Table 4 and 5, for the uniform and L_{UV} stacking, respectively.

We first show the stacked image stamps of the STRONG-[O II] sample — our largest sample consisting of 32 galaxies — as an example of the end products from our stacking analyses elaborated in Sect. 5. The combined images stacked using the L_{UV} weighting of all four filters (F275W, F435W, F606W, and F814W) on the entire 3'' × 3'' spatial extent with 0.''03 plate scale are shown in Fig. 5. The Kron elliptical aperture defined via our PHOTUTILS photometry with the default parameters is shown as the magenta ellipse in each panel in the top row. The 15, 40, and 90 percentiles of the peak flux in each ACS filter are also marked as white contours. We see that our rigorous stacking methodology ensures a centrally concentrated light profile in the three ACS filters that probe the rest-frame UV spectra of the sample galaxy population. The source number counts as shown in the far right panel of Fig. 5 implies a good re-centroiding process during stacking. Similar features of the stacked count map and UV light profiles are seen using the uniform weighting and for other galaxy samples as well.

Our large parent sample size allows us to constrain f_{esc} in three separate redshift bins: the LOW- z sample of $z \in [2.4, 2.5]$ with $z_{\text{median}} = 2.45$, the INTERMEDIATE- z sample of $z \in [2.5, 3.0]$ with $z_{\text{median}} = 2.75$, and the HIGH- z sample of $z \in [3.0, 3.7]$ with $z_{\text{median}} = 3.3$, to account for the rapidly evolving IGM opacity across redshifts. The very similar sample sizes (28, 28, and 29 sources for the LOW- z , INTERMEDIATE- z , and HIGH- z samples, respectively) facilitate a more convenient comparison of the measured UVC to LyC flux ratio and f_{esc} . The stacked image stamps of F275W (covering LyC) and F606W (covering the rest-frame 1500 Å flux as UVC) produced by both stacking methods for the LOW- z , INTERMEDIATE- z , and HIGH- z samples are shown in Figs. 6, 7, and 8, respectively. We obtain 2- σ limits of $\text{mag}_{\text{F275W}} > 29.38$ ABmag and $f_{\text{esc}}^{\text{rel}} < 6.1\%$ for the LOW- z sample stacked using the uniform weighting. On average, the LOW- z sample shows slightly higher dust attenuation of $E(B - V) = 0.21$ than that of the other samples. After correcting for dust, we get a 2- σ upper limit of $f_{\text{esc}}^{\text{abs}} < 0.8\%$. We achieve tighter upper limits of $f_{\text{esc}}^{\text{rel}} < 2.6\%$ and $f_{\text{esc}}^{\text{abs}} < 0.5\%$ for the HIGH- z sample due to the precipitously dropping average IGM transmission at high redshifts, i.e., $\langle \bar{t}_{\text{IGM}} \rangle = 0.06$. The stacking results from the L_{UV} weighting are similar.

From the INTERMEDIATE- z bin, we detect tentative LyC signals with $\text{mag}_{\text{F275W}} = 28.96 \pm 0.37$. It is encouraging to see that both stacking methodologies converge to the same SNR of a 2.9- σ significance. In the bottom panels of Fig. 7, we show the zoom-in views of central 2'' × 2'' regions of the F275W and F606W stacks probing the potential LyC signals and the rest-frame 1,500 Å UVC flux. In the middle panel of both stacking methods, we show the F275W stack smoothed

using a boxcar kernel with a width of 3 pixels, to highlight the potential escaping LyC flux.

To verify the significance of this tentative detection, we conduct random empty aperture analyses as in Prichard et al. (2022). We randomly draw 1,000 circular apertures with a radius of 9 pixels (i.e., $r = 0.''27$, similar to the size of the the Kron aperture employed in stacked image photometry) in empty regions of the F275W stack, with the central region properly masked. As shown in Fig. 9, the distribution of the total fluxes measured within these apertures can be well represented by a Gaussian with a mean of $\mu = 0.0002$ (-0.0002) μJy and a standard deviation of $\sigma = 0.0035$ (0.0047) μJy for the uniform (L_{UV}) stacking method. The vertical lines mark the measured fluxes of the tentative LyC signals of $f_{\nu}=0.0095$ and 0.0132 μJy from the uniform and L_{UV} weighting, respectively, both compatible with the significance reported in Tables 4 and 5. We also find out that the uniform stacking gives slightly smaller noise fluctuations than that by the L_{UV} stacking, and hereafter we refer to the results given by the uniform weighting as our default set of results.

To estimate the sample variance and thus the statistical uncertainty of the inferred escape fractions from our tentative detections, we rely on the bootstrapping technique (as frequently used in cluster lens modeling practices, see e.g., Wang et al. 2015). We randomly drop one galaxy from the stacking sample and re-stack the rest of the sample following the entire procedures outlined in Sect. 5.2. This practice is repeated in a large number of times to provide a range of estimates of the observed UVC/LyC flux ratios and the escape fractions. We take the 16 and 84 percentiles of this range as the $1-\sigma$ statistical uncertainty reported in Tables 4 and 5. As a result, we obtain a relative LyC escape fraction of $f_{\text{esc}}^{\text{rel}} = 10.4\%$ for the INTERMEDIATE- z sample at the median redshift of $z \sim 2.75$, with a bootstrapped $1-\sigma$ uncertainty range of [9.2, 11.3]%. We notice that the INTERMEDIATE- z sample has the smallest sample median dust extinction value ($E(B-V)=0.15$) among the five stacking sub-groups, more favorable to the escape of the ionizing radiation. Assuming $E(B-V)=0.15$, we convert $f_{\text{esc}}^{\text{rel}}$ to $f_{\text{esc}}^{\text{abs}} = 2.4\%$, with a $1-\sigma$ uncertainty range of [2.1, 2.6]% for the INTERMEDIATE- z sample.

Our large sample size enables us to test the strengths of escaping LyC flux as a function of galaxy global properties. We repeat our stacking analysis on the GOLD- z sample, comprising galaxies in the first and second redshift quality quintiles ranked by our dedicated visual inspection efforts, considered to have the most secure spectroscopic redshifts. There are 26 galaxies in the GOLD- z sample, with a median redshift of $z \sim 2.57$. The presence of escaping LyC in this sample is not detected in the F275W stacks (see Fig. 10). We obtain $2-\sigma$ lower limits of $\text{mag}_{\text{F275W}} > 29.35$ ABmag and $\left(\frac{F_{\text{UVC}}}{F_{\text{LyC}}}\right)_{\text{obs}} > 54.15$. This is equivalent to $2-\sigma$ upper limits of

$f_{\text{esc}}^{\text{rel}} < 4.9\%$ and $f_{\text{esc}}^{\text{abs}} < 0.9\%$ assuming the sample median $E(B-V)=0.18$.

These non-detections of F275W flux might stem from the small number of galaxies included in stacking for the above three samples, or the CTE degradation effect. Yet the latter seems unlikely since the LyC stacks from Smith et al. (2020) show no evidence of CTE effects when comparing the pristine WFC3/UVIS ERS data (Windhorst et al. 2011) to the later observed HDUV data (Oesch et al. 2018), which is more prone to CTE degradation. These stringent upper limits from stacking non-detections and the high lower limits of LyC escape fractions estimated for the three tentative individual LyC leakers presented in Table 3 confirm the intriguing bimodality of f_{esc} at high redshifts (see also similar conclusion found by the LACES program, *HST*-GO-14747; P.I. Robertson, Fletcher et al. 2019).

Finally we perform stacking and photometry on the STRONG-[O II] sample. Thanks to the wide coverage of the *HST* WFC3/G141 slitless spectroscopy in the UVCANDELS fields, the vast majority of our galaxies have rest-frame near-UV and optical SED measured by G141. The redshift cut imposed by our original sample selection (i.e. $z \gtrsim 2.4$) precludes our access to some frequently used strong rest-frame optical nebular emission lines, e.g., H α , [O III]. The only strong line covered by G141 at this redshift range is [O II]. As such, we take advantage of the CHARGE initiative that reanalyzes all the existing *HST* NIR imaging and slitless spectroscopy in our fields, to obtain the flux, $1-\sigma$ uncertainty, equivalent width of [O II] for our galaxies, as briefly mentioned in Sect. 4.2. This STRONG-[O II] subsample consists of 32 strong emission-line galaxies at a median redshift of $z \sim 2.65$. As in the INTERMEDIATE- z sample, we also tentatively detect the LyC signals in the F275W stacks (see Fig. 11): $\text{mag}_{\text{F275W}} = 29.07 \pm 0.37$ at $2.9-\sigma$, equivalent to a relative (absolute) LyC escape fraction of 5.7 (1.0)%. This significance is verified in our random empty aperture analysis shown in Fig. 12. From the bootstrapping procedure described above, we estimate the following $1-\sigma$ uncertainty ranges: $f_{\text{esc}}^{\text{rel}} \in [5.1, 6.2]\%$ and $f_{\text{esc}}^{\text{abs}} \in [0.9, 1.1]\%$. The constraints on $f_{\text{esc}}^{\text{rel}}$ from both the INTERMEDIATE- z and the STRONG-[O II] samples (i.e. on the level of 5-10%) are generally compatible with some recent findings by Saxena et al. (2021); Begley et al. (2022); Griffiths et al. (2022), as well as the the result found by the KLCS program, which measures $f_{\text{esc}}^{\text{rel}} = 0.13 \pm 0.04$, from a sample of 106 Lyman-break selected galaxies showing non-detections in Keck/LRIS U-band spectroscopy (Steidel et al. 2018). This supports that galaxies with strong nebular emission in addition to those showing Lyman-break are good candidates to leak ionizing radiation, as they experience prodigious instantaneous star-forming activities, and therefore excellent analogs of the first

galaxies that drive cosmic reionization (Tang et al. 2019; Endsley et al. 2021).

The bottom panels of Fig. 11 shows the zoom-in views of central regions of the F275W stacks, where this tentative escaping LyC signals are seen. Intriguingly, we see that the morphology of this tentative LyC signal does not resemble that of the population-averaged UVC light. Similar phenomena have been reported in individual prodigious LyC leakers (see e.g., Vanzella et al. 2016; Ji et al. 2020; Vanzella et al. 2022). Because dust and neutral hydrogen in the ISM are highly efficient in absorbing the LyC radiation, the escape of the ionizing radiation benefits from the low covering fraction of the ISM (Jaskot & Oey 2013). Indeed, cosmological hydrodynamic simulations predict that the LyC radiation has better chances to escape from their host galaxies via low column density paths pre-cleared by feedback and fully ionized by young O-type stars recently formed in this region (Ma et al. 2020). Our careful recentroiding methodology before stacking entails centering of the H α regions with high ISM covering fraction and the bulk UVC flux emitted by massive stars; this naturally suppresses the emergence of LyC flux from the center of the stacks. Our finding, in accord with the conclusion drawn from the observations of individual LyC leakers and numerical simulations, strongly suggests that the clumpy ISM geometry with non-uniform covering fraction is highly conducive to the escape of LyC flux.

7. CONCLUSIONS

In this paper, we introduce the *UVCANDELS HST* Cycle-26 Treasury Program (*HST*-GO-15647, PI: Teplitz), awarded in total 164 orbits of primary WFC3/F275W and coordinated parallel ACS/F435W imaging observations. Its wide sky coverage of ~ 426 arcmin 2 , a factor of 2.7 larger than all previous *HST* UV data combined, makes it the largest space-based UV sky survey of distant galaxies with high angular resolution. We present its first set of science-enabling data products — the coadded imaging mosaics publicly released at <https://archive.stsci.edu/hlsp/uvcandels> — together with an in-depth description of the data reduction procedures. These mosaics are astrometrically aligned to the *CANDELS* world-coordinate system. The data processing is designed to overcome the issues affecting the quality of UVIS imaging: the CTE degradation, readout cosmic ray corrections, epoch-varying scattered light during the CVZ observations, etc. As a highlight of the research potential of the *UVCANDELS* dataset, we focus on one particular application of these imaging mosaics, i.e., searching for strong individual star-forming galaxies that leak LyC radiation and constraining the LyC escape fraction through stacking non-detections.

Our main conclusion is summarized as follows.

- We build a large compilation of currently existing spectroscopic data sets in the *CANDELS* fields and or-

ganize dedicated visual inspection efforts to vet the quality of the rest-frame UV/optical spectra for sources at $2.4 \lesssim z \lesssim 3.7$, to exclude spurious spectroscopic redshift measurements. We identify a sample of five galaxies as likely individual LyC leaker candidates, as they show tentative detections ($\text{SN}_{\text{F275W}} \geq 3$) in the *UVCANDELS* F275W imaging. Deeper UV imaging and spectroscopic observations at high angular resolution can be helpful in characterize the detailed properties (e.g. morphology) of these escaping LyC signals.

- We design a rigorous and efficient image stacking methodology using two weighting schemes: the uniform and L_{UV} weighting. Our stacking method is capable of properly recentroiding cutout stamps in terms of source optical/UV isophotes, masking any possible neighboring contaminants, and subtracting local residual sky backgrounds to the level of 10^{-4} μJy .
- We apply our stacking method to three separate redshift bins: the LOW- z , INTERMEDIATE- z , and HIGH- z samples, consisting of 28, 28, and 29 galaxies, respectively. All these galaxies show non-detections in F275W by themselves but have secure spectroscopic redshifts. We also perform stacking of the GOLD- z sample with the best quality of spectroscopic redshifts from our dedicated visual inspection. We measure a tentative stacked LyC signal of $\text{mag}_{\text{F275W}} = 28.96 \pm 0.37$ in the INTERMEDIATE- z bin at a $2.9\text{-}\sigma$ confidence level. This is equivalent to $f_{\text{esc}}^{\text{rel}} = 10.4\%$ at the sample median redshift of $z \sim 2.75$, with a $1\text{-}\sigma$ uncertainty range of [9.2, 11.3]%. The non-detections in the other samples, combined with the high escape fractions for the individual leaker candidates, confirm the strong bimodality seen in high- z LyC escape fraction estimates.
- The stacks of the strong emission-line galaxies also show tentative LyC detection of $\text{mag}_{\text{F275W}} = 29.07 \pm 0.37$ at $2.9\text{-}\sigma$. This translates into $f_{\text{esc}}^{\text{rel}} = 5.7\%$ with a $1\text{-}\sigma$ uncertainty range of [5.1, 6.2]%, at the sample median redshift of $z \sim 2.65$. This advocates for the prevalent role of strong line emitters in causing the cosmic reionization and maintaining the UV ionization background. We find that the morphology of the tentative LyC signals in F275W stacks is different from the highly concentrated UVC light profile in the F606W stacks. This is consistent with the observations of currently known individual prodigious LyC leakers and numerical simulations, in support of the argument that the non-uniform ISM covering fraction is conducive to the escape of LyC flux.

As summarized in Sect. 2, constraining the escape fraction of the ionizing radiation from galaxies and AGNs at $z \gtrsim 2.4$

(see our companion work of Smith et al. 2023, in prep., for the stacking analysis of AGNs using similar methodology) is merely one of the five major science goals of the UVCANDELS program. The unique UV/optical dataset produced and publicly released by the UVCANDELS team will offer tremendous opportunities of scientific explorations on various aspects of galaxy formation and evolution. The science-enabling data products will also support the near and mid infrared observations from the JWST in these legacy extragalactic survey fields.

1 This work is based on observations with the NASA/ESA
 2 Hubble Space Telescope obtained at the Space Telescope
 3 Science Institute, which is operated by the Association of
 4 Universities for Research in Astronomy, Incorporated, under
 5 NASA contract NAS5- 26555. Support for Program number
 6 HST-GO-15647 was provided through a grant from the
 7 STScI under NASA contract NAS5-26555. XW acknowl-
 8 edges work carried out, in part, by IPAC at the California
 9 Institute of Technology, and was sponsored by the National
 10 Aeronautics and Space Administration. XW is supported by
 11 the Fundamental Research Funds for the Central Universi-
 12 ties, and the CAS Project for Young Scientists in Basic Re-
 13 search, Grant No. YSBR-062. RAW acknowledges support
 14 from NASA JWST Interdisciplinary Scientist grants NAG5-
 15 12460, NNX14AN10G and 80NSSC18K0200 from GSFC.
 16 We thank A. Barger and N. Reddy for providing the reduced
 17 spectra of their Keck observations useful for our visual in-
 18 spection efforts. We acknowledge A. Inoue for providing the
 19 line-of-sight Monte Carlo IGM transmission code.

Software: SExtractor (Bertin & Arnouts 1996), CIGALE Boquien et al. (2019), PHOTUTILS (Bradley et al. 2022), GRIZLI (Brammer & Matharu 2021), ASTRODRIZZLE (Hack et al. 2021), PYRAF (Science Software Branch at STScI 2012), the line-of-sight Monte Carlo IGM transmission code by Inoue et al. (2014).

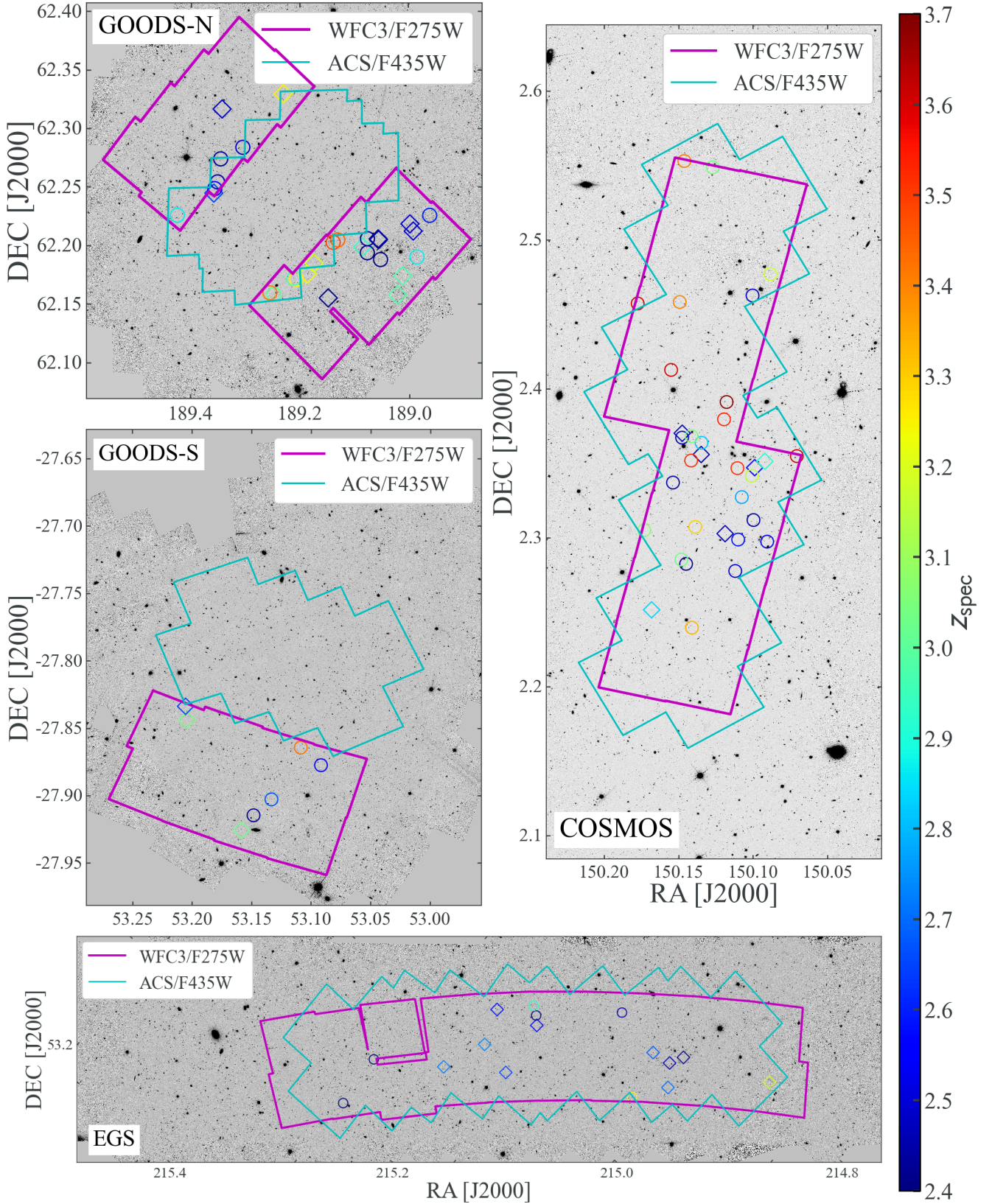


Figure 1. The *UVCANDELS* survey footprints overlaid on top of the F814W mosaics of the four premier CANDELS fields: GOODS-N, GOODS-S, EGS, and COSMOS (Grogin et al. 2011; Koekemoer et al. 2011). Small chip gaps of the WFC3 and ACS detectors are not shown from the *UVCANDELS* footprints. We also highlight the galaxies selected for the stacking analysis elaborated in Sect. 5. They are color-coded in their spectroscopic redshifts visually inspected in Sect. 4. The diamonds represent the stacking galaxy sample which show significant [O II] emission (see Table 2), while the rest of the sample are denoted by circles. The same color-coding and symbol style are utilized in all four panels.

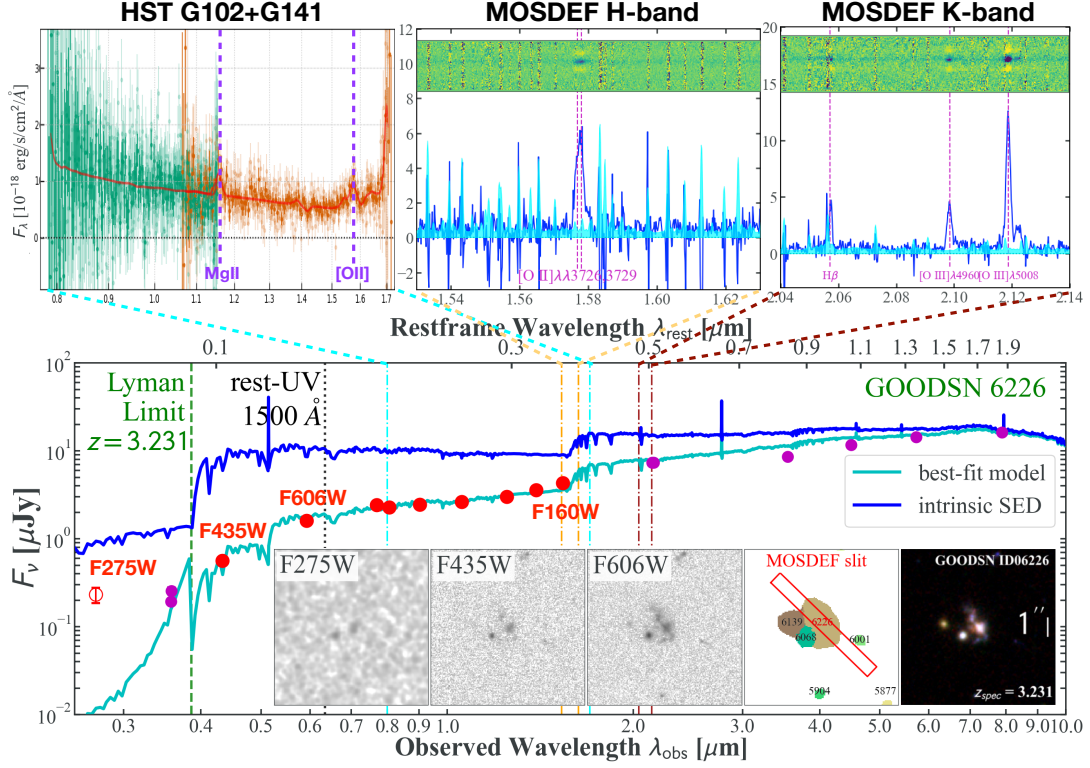


Figure 2. Galaxy ID 6226 at $z = 3.23$ in the GOODS-N field, one example of our tentative individual LyC leakers. **Top:** the spectra of ID 6226 taken from *HST* G102+G141 slitless spectroscopy and MOSDEF (in H and K bands), showing strong emission features marked by the vertical dashed lines in magenta. The orientation of the MOSDEF slit is shown in the segmentation map displayed in the bottom row. **Bottom:** The extensive multi-band photometry from *HST* (red dots) and other telescopes (magenta dots) constrains its SED (cyan curve: best-fit model from CIGALE, Boquien et al. 2019) to high precision. We do not include the measured F275W flux (represented by the hollow red dot) in the fit to avoid assuming the average IGM attenuation by CIGALE (see Sect. 5.1 for more details). The intrinsic galaxy SED without IGM attenuation or dust extinction is shown in the blue curve. Given its secure spectroscopic redshift ($z = 3.23$), our F275W imaging captures its LyC signal over the restframe wavelength range of $\lambda_{\text{rest}} \in [570, 730]$ Å at high significance, i.e., $\text{mag}_{\text{F275W}} = 25.5$ ABmag at 5σ (see Table 3). **Bottom inset:** multi-wavelength (F275W, F435W, F606W) postage stamps obtained by *HST*, the F160W segmentation map, and the color-composite image produced from *HST* imaging. The F275W stamp is smoothed by a boxcar kernel with a width of $0''.1$ to highlight the detection.

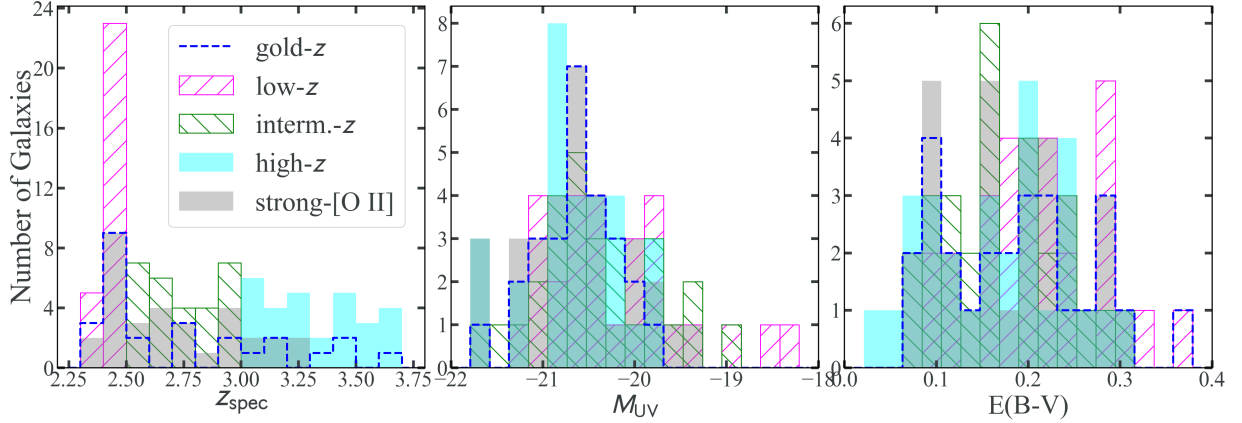


Figure 3. Distribution of spectroscopic redshifts (z_{spec}), absolute UV magnitude (M_{UV}) and dust attenuation ($E(B-V)$) of the selected stacking samples. The median values of these three key properties for each sample are as follows. STRONG-[O II]: $z_{\text{median}} = 2.65$, $M_{\text{UV}} = -20.6$, $E(B-V) = 0.18$. LOW- z : $z_{\text{median}} = 2.45$, $M_{\text{UV}} = -20.4$, $E(B-V) = 0.21$. INTERMEDIATE- z : $z_{\text{median}} = 2.75$, $M_{\text{UV}} = -20.5$, $E(B-V) = 0.15$. HIGH- z : $z_{\text{median}} = 3.3$, $M_{\text{UV}} = -20.7$, $E(B-V) = 0.17$. GOLD- z : $z_{\text{median}} = 2.71$, $M_{\text{UV}} = -20.6$, $E(B-V) = 0.18$. The total number of galaxies in the STRONG-[O II], LOW- z , INTERMEDIATE- z , HIGH- z , and GOLD- z stacking samples are 32, 28, 28, 29, and 26 respectively. The numbers counts of each sample within individual fields are broken down in Table 2.

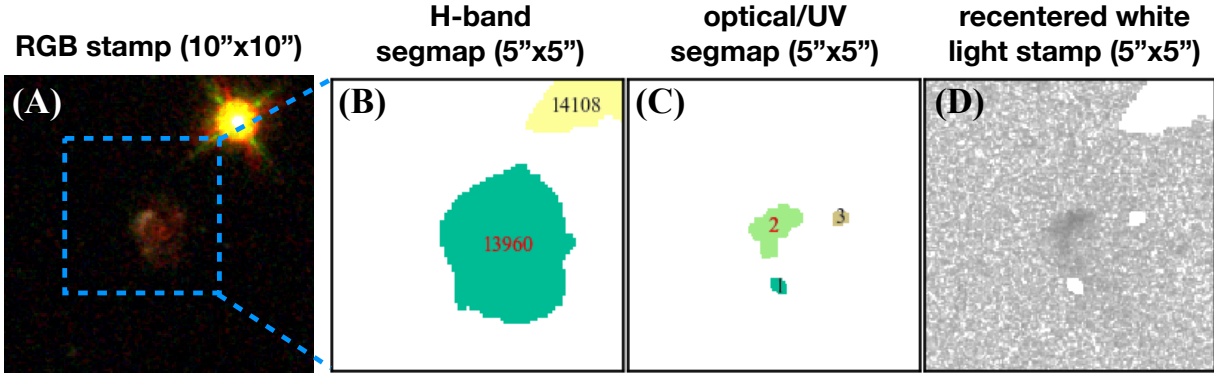


Figure 4. An illustration of our re-centroiding and contaminant-masking methodology via performing stamp photometry before the stacking analysis. **(A)** galaxy color-composite stamp with size $10'' \times 10''$ made from the *CANDELS* near-infrared and optical imaging, centered on the F160W light centroid. The blue dashed square ($5'' \times 5''$) marks the spatial extent of panels **(B)-(D)**, which are all the same. **(B)** *CANDELS* F160W segmentation map defined using the hot+cold source detection scheme (see e.g., Guo et al. 2013). The ID of our source of interest is marked in red, while the ID of a neighbouring source (a star spike) in black. **(C)** optical/UV segmentation map using the white light image as detection image, while masking all neighbouring sources. The region #2 has the brightest F435W flux, so the light centroid of region #2 is used to re-center panels **(B)-(D)**. **(D)** the white light image stamp with neighbouring sources and segmented regions within our source of interest (i.e. regions #1 and #3) masked. Here we clearly see that the light centroids of optical/UV and near-infrared bands do not overlap. These possible offsets can be effectively accounted for using our re-centroiding and contaminant-masking methodology.

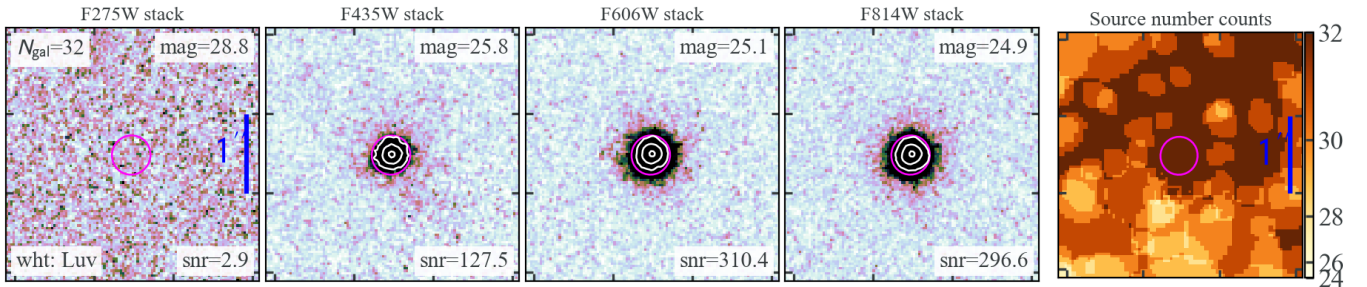


Figure 5. The stacked image stamps in filters F275W, F435W, F606W, and F814W for the STRONG-[O II] galaxy sample at a sample median redshift of $z \sim 2.65$. This galaxy sample consists of 32 sources in the redshift range of $z \in [2.4, 3.2]$, all showing strong [O II] nebular emission in their G141 grism spectra. We achieve a tentative LyC detection at $2.9\text{-}\sigma$ confidence level for this sample. **(Left four panels):** the stacked flux stamps created using the L_{UV} weighting scheme prescribed in Eq. 2. All stamps have $3'' \times 3''$ and a plate scale of $0.''03$. The magenta ellipse overlaid marks the Kron elliptical aperture defined using the F435W stack as detection image (see Sect. 5.3 for more details). The auto magnitude and its SNR measured within the Kron aperture are shown in each panel. The white contours overlaid in filters F435W, F606W, and F814W correspond to the 15, 40, and 90 percentiles of the peak flux in respective filter, to highlight the good performance of our re-centroiding procedure elaborated in Sect. 5.2. **(Right most panel):** the number count map showing the number of individual sources contributing to each one of the spatial pixels. The number reaches 32 in the center indicating a good re-centroiding process before the stacking. The deficit in the outskirts of the source count map comes from masked nearby neighbors of individual galaxies.

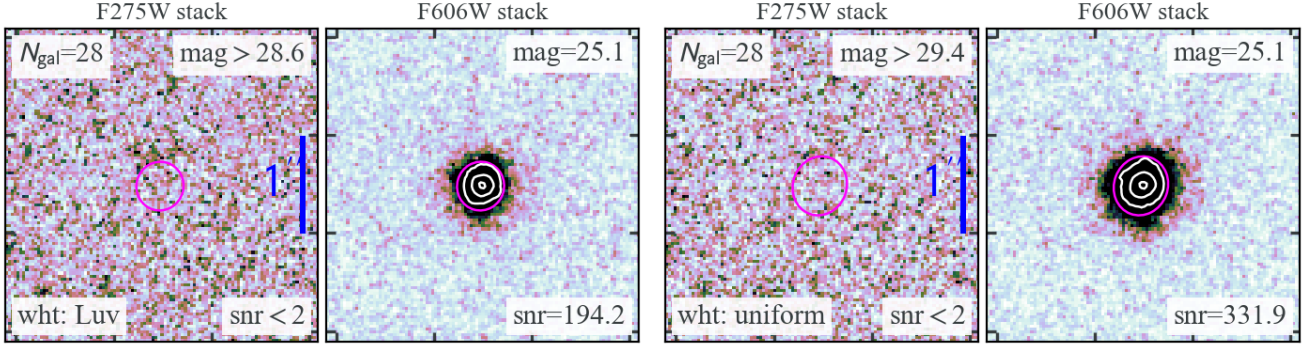


Figure 6. The stacked image stamps in filters F275W and F606W for the low- z galaxy sample comprising 28 sources at a median redshift of $z \sim 2.45$. The stacks created using the L_{UV} weighting are shown on the left, while those using the uniform weighting on the right. As shown in Fig. 5, the magenta ellipse corresponds to the Kron aperture for photometry with measurements presented in each panel. The white contours overlaid mark the 15, 40, and 90 percentiles of the peak flux in respective filter. The F275W stacks show non-detection, and we present a $2\text{-}\sigma$ lower limit of $\text{mag}_{\text{F275W}} > 28.64$ and $\text{mag}_{\text{F275W}} > 29.38$, for the L_{UV} and uniform weighting results, respectively.

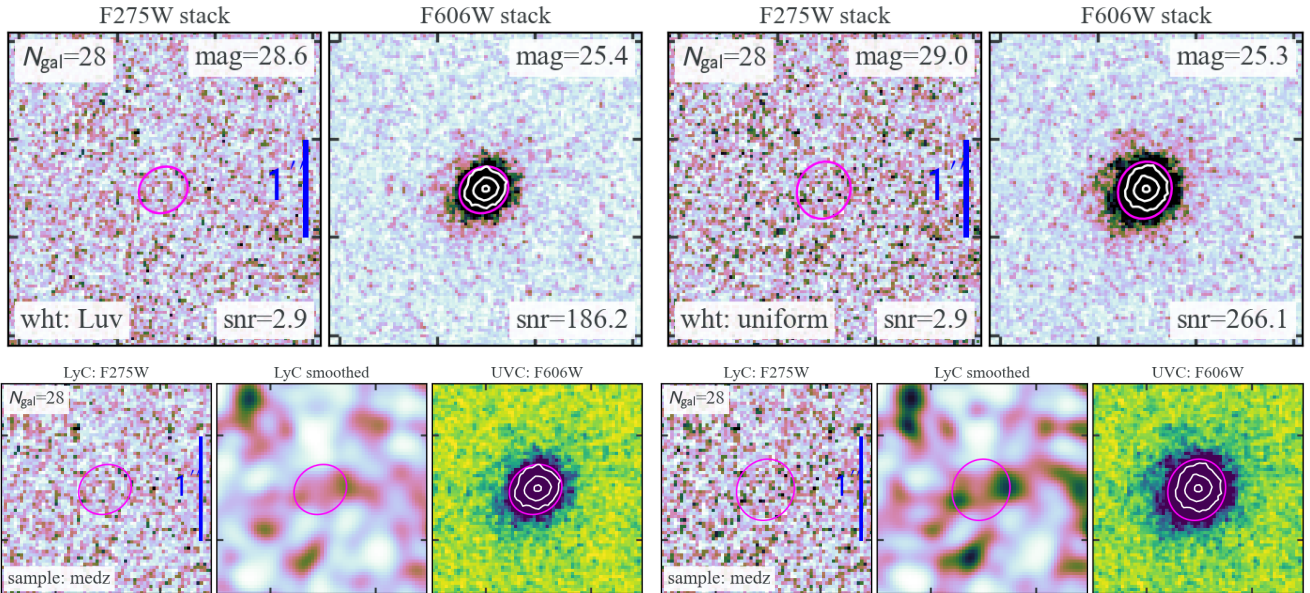


Figure 7. The stacked image stamps in filters F275W and F606W for the INTERMEDIATE- z galaxy sample comprising 28 sources at a median redshift of $z \sim 2.75$. The top panels follows the figure format of Fig. 6. We measure a tentative signal of $\text{mag}_{\text{F275W}} = 28.60$ and $\text{mag}_{\text{F275W}} = 28.96$ at $2.9\text{-}\sigma$ confidence level from both stacking methods. The bottom panels present a zoom-in view of the stacked LyC (F275W) and UVC (F606W) stamps ($2'' \times 2''$) given by the L_{UV} weighting on the left and the uniform weighting on the right. In the middle panel of both sides, we also show the LyC stamp smoothed using a boxcar kernel with a width of 3 pixels, to highlight the potential LyC signals.

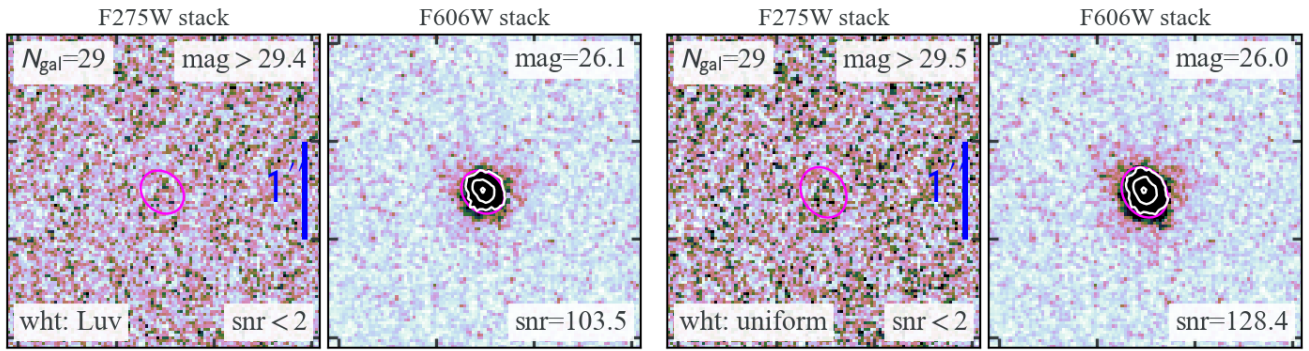


Figure 8. The stacked image stamps in filters F275W and F606W for the high- z galaxy sample comprising 29 sources at a median redshift of $z \sim 3.3$. The figure format follows that of Fig. 6. The F275W stacks show non-detection, and we present a $2\text{-}\sigma$ lower limit of $\text{mag}_{\text{F275W}} > 29.36$ and $\text{mag}_{\text{F275W}} > 29.52$, for the L_{UV} and uniform weighting results, respectively.

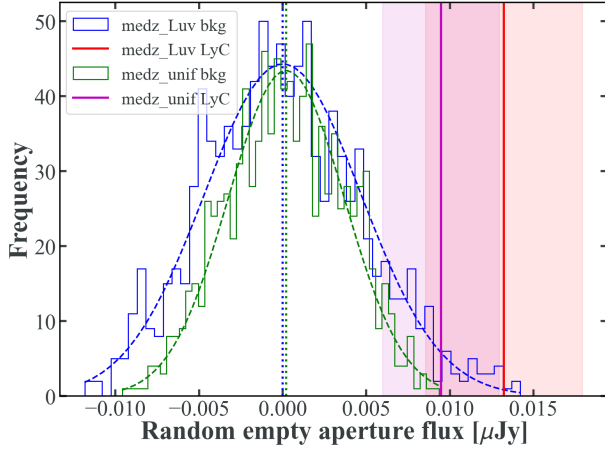


Figure 9. The histograms of background fluxes measured within a large number of circular apertures randomly drawn from empty regions in the F275W stack for the INTERMEDIATE- z sample. The size of these empty apertures ($r = 0''.27$) is taken to be almost identical to that of the Kron aperture shown in Fig. 7. The Gaussian fit yields a mean value of $\mu = 0.0002$ (-0.0002) μJy and a standard deviation of $\sigma = 0.0035$ (0.0047) μJy for the uniform (L_{UV}) weighting method, indicating well-defined noise properties and sufficiently clean local sky background. The magenta (red) vertical line marks our observed tentative LyC signal with an auto flux of 0.0095 (0.0132) μJy measured from the uniform (L_{UV}) weighting. The shaded bands represent the corresponding $\pm 1\text{-}\sigma$ standard deviation range.

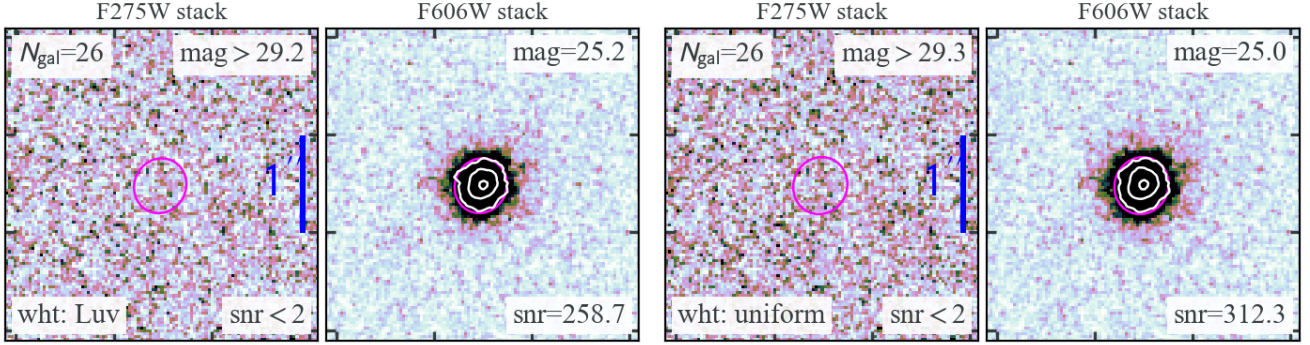


Figure 10. The stacked image stamps in filters F275W and F606W for the GOLD- z galaxy sample comprising 26 sources at a median redshift of $z \sim 2.57$. The figure format follows that of Fig. 6. The F275W stacks show non-detection, and we present a $2\text{-}\sigma$ lower limit of $\text{mag}_{\text{F275W}} > 29.25$ and $\text{mag}_{\text{F275W}} > 29.35$, for the L_{UV} and uniform weighting results, respectively.

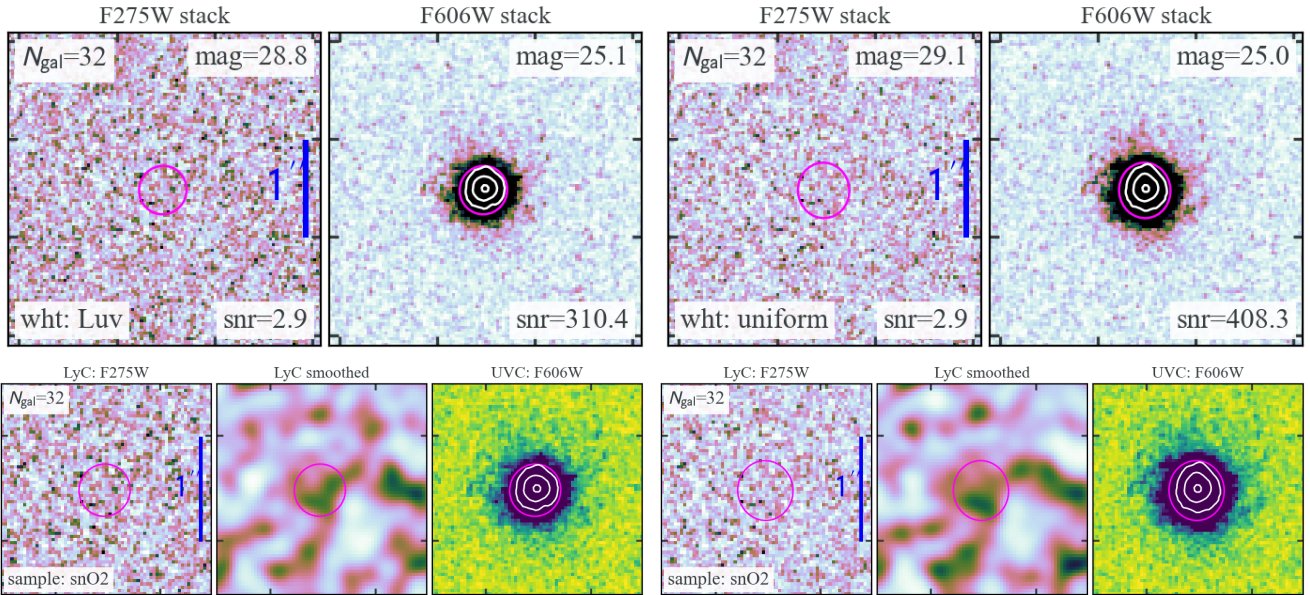


Figure 11. The stacked image stamps in filters F275W and F606W for the STRONG-[O II] galaxy sample comprising 32 sources at a median redshift of $z \sim 2.65$ each showing strong [O II] nebular emission in their G141 grism spectra. The top panels follows the figure format of Fig. 6. The stacked LyC signal is tentatively detected at $2.9\text{-}\sigma$ confidence level of $\text{mag}_{\text{F275W}} = 28.82$ and $\text{mag}_{\text{F275W}} = 29.07$. Similar to Fig. 7, the bottom panels present a zoom-in view of the stacked LyC (F275W) and UVC (F606W) stamps ($2'' \times 2''$), with the middle panel on both sizes showing the smoothed LyC stamp, to highlight the potential LyC signals.

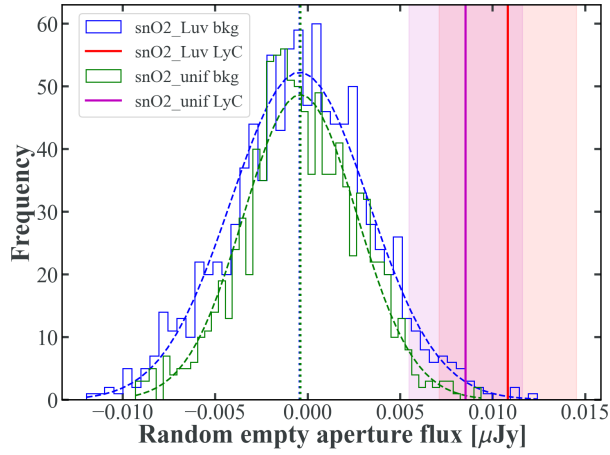


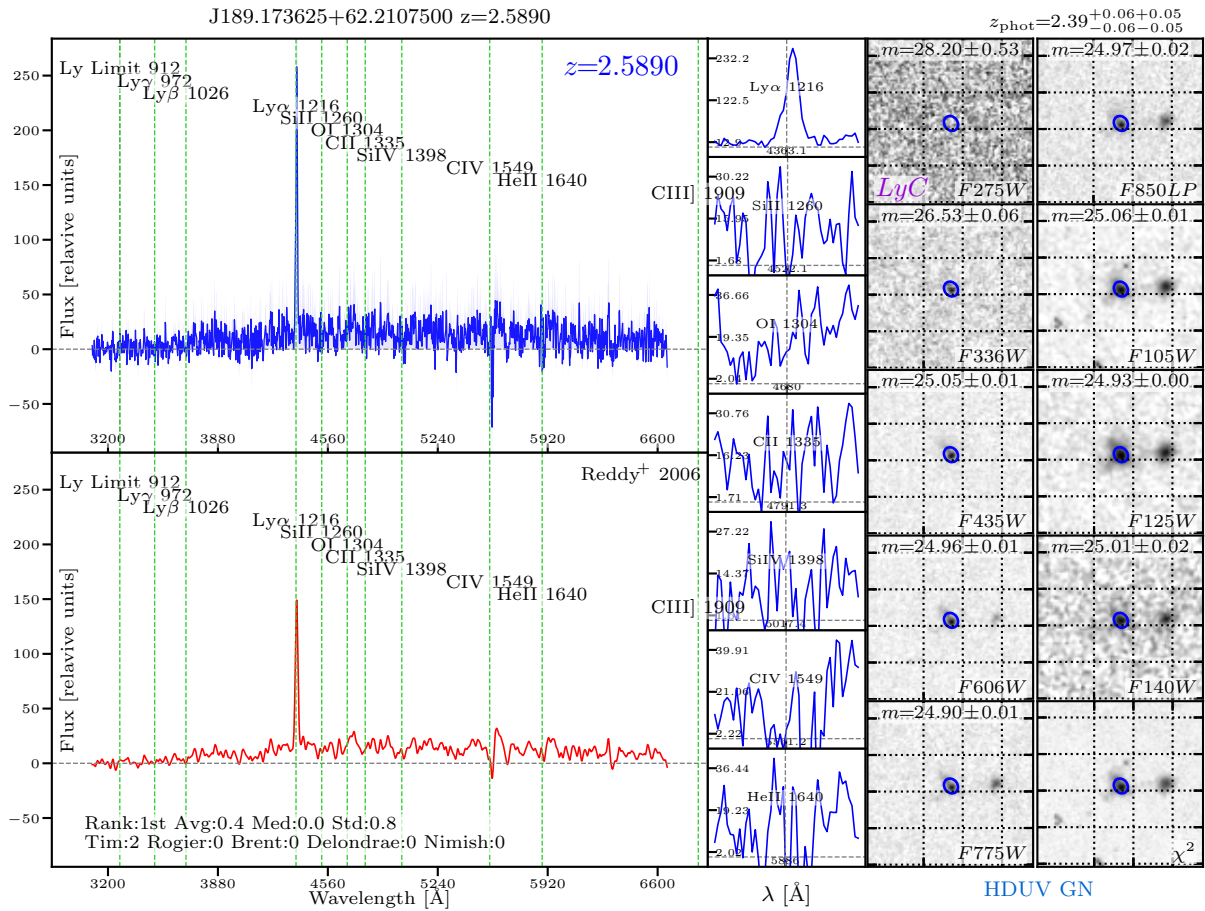
Figure 12. The histograms of background fluxes measured within a large number of circular apertures randomly drawn from empty regions in the F275W stack for the `STRONG-[O II]` sample. The size of these empty apertures ($r = 0.''27$) is taken to be almost identical to that of the Kron aperture shown in Fig. 7. The Gaussian fit yields a mean value of $\mu = -0.0004$ (-0.0004) μJy and a standard deviation of $\sigma = 0.0030$ (0.0037) μJy for the uniform (L_{UV}) weighting method, indicating well-defined noise properties and sufficiently clean local sky background. The magenta (red) vertical line marks our observed tentative LyC signal with an auto flux of 0.0085 (0.0108) μJy measured from the uniform (L_{UV}) weighting. The shaded bands represent the corresponding $\pm 1\text{-}\sigma$ standard deviation range.

APPENDIX

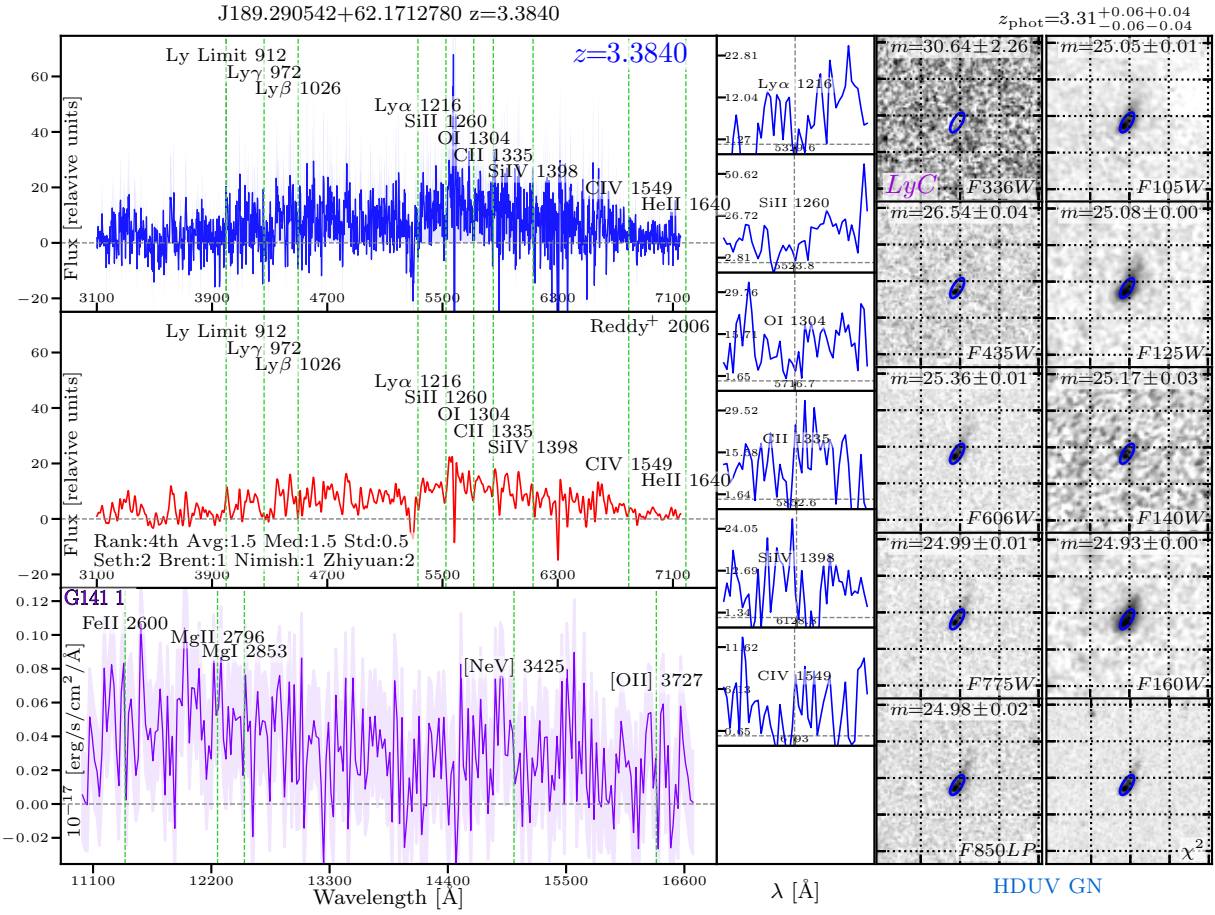
A. EXAMPLE FIGURES USED FOR VISUAL CONFIRMATION OF SPECTROSCOPIC REDSHIFT

As discussed in Sect. 4.2, we visually confirmed the spectroscopic redshift of the galaxies in our sample since some ground based spectra are prone to noise and limited by seeing conditions. Here, we show an example figure of a galaxy that was ranked into each quintile. The blue curve is the spectrum obtained directly from the archive of the referenced literature source, and the red curve is the same curve convolved with a $\sigma = 3 \text{ \AA}$ wide Gaussian. Several regions of the spectra where emission/absorption lines are expected are shown in greater detail for inspection of the line profiles. The z_{phot} shown is taken from Skelton et al. (2014). HST image cutouts filter bands are indicated in their own panels, with the LyC filter distinguished. The original HST mosaics where the image cutouts were extracted from is indicated in blue text below all the image cutouts displayed. The χ^2 image refers to images constructed as described in Szalay et al. (1999). Individual ranks are shown for several co-authors, as well as the average, median, and standard deviation of these values.

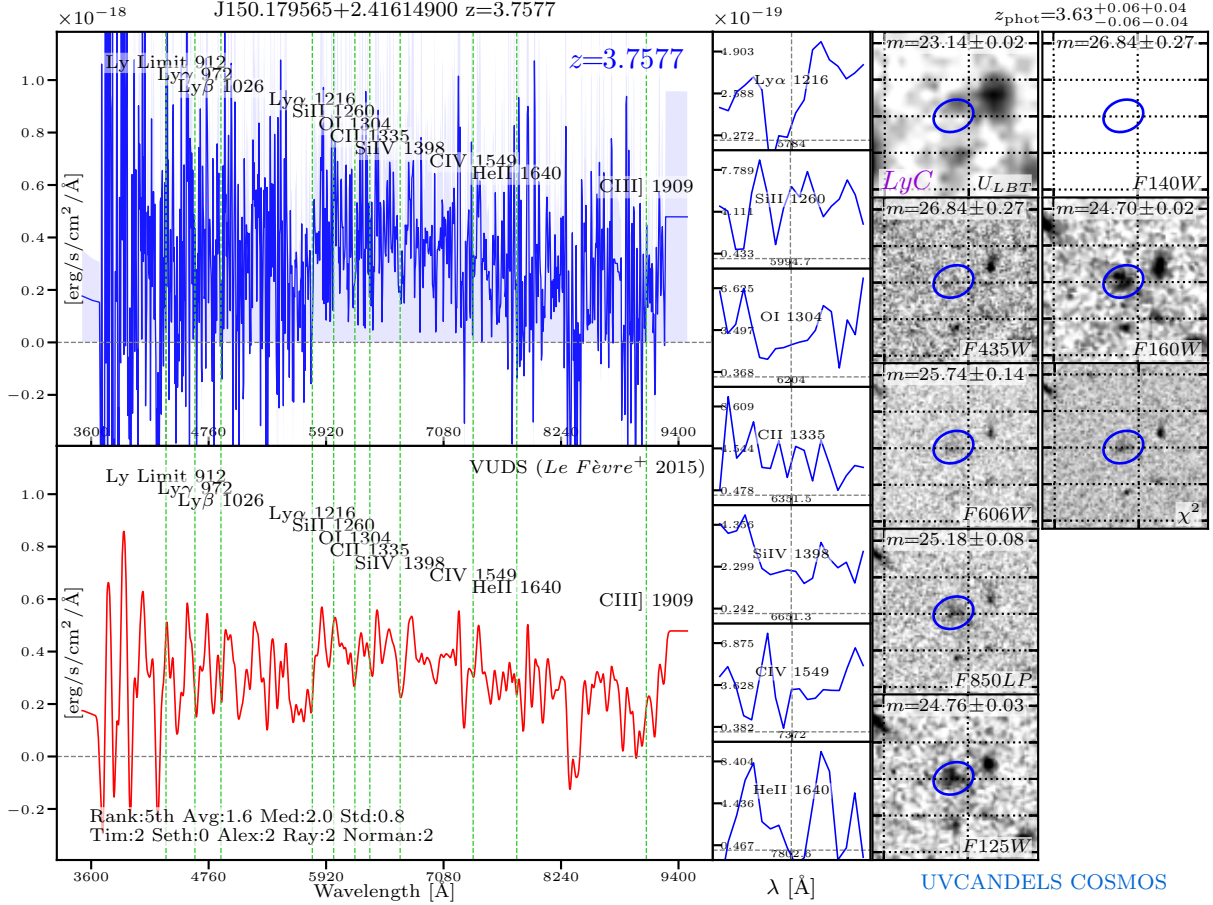
A.1. 1st quintile



A.4. 4th quintile



A.5. 5th quintile



B. SPECTRA, HST IMAGE CUTOUTS, AND SEDS OF ADDITIONAL LYC LEAKER CANDIDATES

In total, five galaxies are identified from the catalog of high-quality spectroscopic redshifts within the *UVCANDELS* survey footprints, which show relatively strong detection in F275W (e.g. $\text{SNR} \geq 3$) and in the redshift range of $z \in [2.4, 3.7]$, where F275W probes their escaping LyC flux. The archival spectra, taken from ground-based and/or *HST* grism instruments (Reddy et al. 2006; Barger et al. 2008; Kriek et al. 2015; Kokorev et al. 2022), for four of the five sources are shown in the left panels of Figs. 13-16, with the remaining one already shown in Fig. 2. For high-resolution spectroscopy taken with Keck, we show both the original (blue) and the smoothed version using a $3\text{-}\sigma$ Gaussian kernel (red). The image stamps of filters F275W (smoothed with a $3\text{-}\sigma$ Gaussian kernel), F435W, and F606W, the F160W segmentation maps, and the color composite images of these galaxies are displayed in the lower right panels of each figure.

We conduct detailed SED fitting using the CIGALE software to obtain the intrinsic SED of these galaxies before IGM and ISM absorption, with results shown in the upper right panels of each figure. Following the presentation of Fig. 2, the multi-band photometry includes those secured by *HST* (red dots) and other channels (e.g., Spitzer IRAC and ground-based imaging, shown in magenta dots). The F275W imaging (hollow red dots) is not used in our CIGALE fitting analysis, since we do not apply the average IGM correction to fit galaxy's SED. The cyan curves correspond to the best-fit SEDs that accurately reproduce the observed photometric data points, whereas the blue curves show the intrinsic SED without Lyman series absorption from the galaxy ISM and the IGM. We then perform MC simulations using the Inoue et al. (2014) prescription to apply line-of-sight IGM attenuation to the intrinsic SED of our galaxies, to compute f_{esc} given in Table 3.

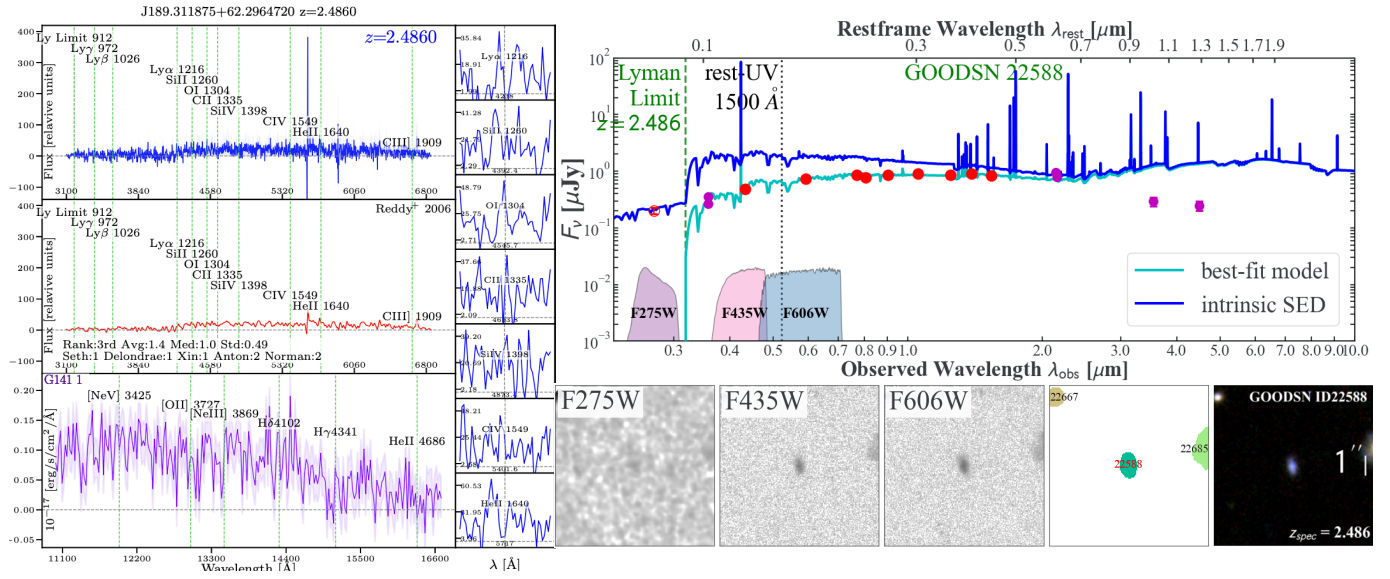


Figure 15. Spectra (left panels), HST image stamps (lower right panels), and SEDs (upper right panels) of galaxy GOODSN ID 22588 at $z_{\text{spec}} = 2.486$.

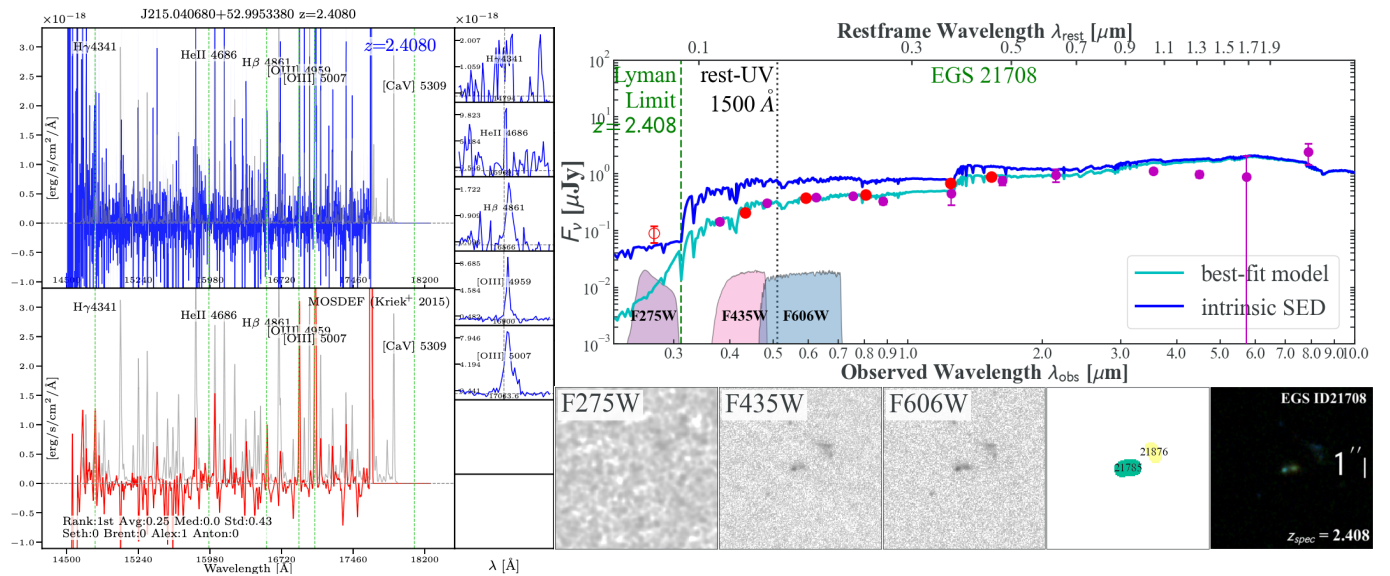


Figure 16. Spectra (left panels), HST image stamps (lower right panels), and SEDs (upper right panels) of galaxy EGS ID 21708 at $z_{\text{spec}} = 2.408$.

REFERENCES

- Alavi, A., Siana, B. D., Richard, J., et al. 2014, *ApJ*, 780, 143, doi: [10.1088/0004-637x/780/2/143](https://doi.org/10.1088/0004-637x/780/2/143)
- Alavi, A., Colbert, J. W., Teplitz, H. I., et al. 2020, *The Astrophysical Journal Letters*, 904, 59, doi: [10.3847/1538-4357/abbd43](https://doi.org/10.3847/1538-4357/abbd43)
- Anderson, J., Baggett, S., & Kuhn, B. 2021, Updating the WFC3/UVIS CTE model and Mitigation Strategies, Instrument Science Report 2021-9, 44 pages
- Ashcraft, T. A., Windhorst, R. A., Jansen, R. A., et al. 2018, *PASP*, 130, 064102, doi: [10.1088/1538-3873/aab542](https://doi.org/10.1088/1538-3873/aab542)
- Balestra, I., Mainieri, V., Popesso, P., et al. 2010, *A&A*, 512, A12, doi: [10.1051/0004-6361/200913626](https://doi.org/10.1051/0004-6361/200913626)
- Barger, A. J., Cowie, L. L., & Wang, W.-H. 2008, *ApJ*, 689, 687, doi: [10.1086/592735](https://doi.org/10.1086/592735)
- Barro, G., Pérez-González, P. G., Cava, A., et al. 2019, *ApJS*, 243, 22, doi: [10.3847/1538-4365/ab23f2](https://doi.org/10.3847/1538-4365/ab23f2)
- Barros, S. d., Vanzella, E., Amorín, R., et al. 2016, *A&A*, 585, A51, doi: [10.1051/0004-6361/201527046](https://doi.org/10.1051/0004-6361/201527046)
- Bassett, R., Ryan-Weber, E. V., Cooke, J., et al. 2021
- Begley, R., Cullen, F., McLure, R. J., et al. 2022, arXiv
- Bergvall, N., Zackrisson, E., Andersson, B.-G., et al. 2006, *Astronomy & Astrophysics*, 448, 513, doi: [10.1051/0004-6361:20053788](https://doi.org/10.1051/0004-6361:20053788)
- Bertin, E., & Arnouts, S. 1996, *Astronomy and Astrophysics Supplement Series*, 117, 393, doi: [10.1051/aas:1996164](https://doi.org/10.1051/aas:1996164)
- Bian, F.-Y., Fan, X., McGreer, I. D., Cai, Z., & Jiang, L.-H. 2017, *ApJ*, 837, L12, doi: [10.3847/2041-8213/aa5ff7](https://doi.org/10.3847/2041-8213/aa5ff7)
- Biretta, J., van Orsow, D., Sparks, W., Reinhart, M., & Vick, A. 2003, ACS Background Light vs. Bright Earth Limb Angle, Instrument Science Report ACS 2003-05, 13 pages
- Boquien, M., Burgarella, D., Roehly, Y., et al. 2019, *A&A*, 622, A103, doi: [10.1051/0004-6361/201834156](https://doi.org/10.1051/0004-6361/201834156)
- Borthakur, S., Heckman, T., Leitherer, C., & Overzier, R. A. 2014, *Science*, 346, 216, doi: [10.1126/science.1254214](https://doi.org/10.1126/science.1254214)
- Bradley, L., $\text{Sip}H_{160}$ ocs, B., Robitaille, T., et al. 2022, *astropy/photutils: 1.5.0*, 1.5.0, Zenodo, doi: [10.5281/zenodo.6825092](https://doi.org/10.5281/zenodo.6825092)
- Brammer, G. B., & Matharu, J. 2021, doi: [10.5281/zenodo.5012699](https://doi.org/10.5281/zenodo.5012699)
- Brammer, G. B., Dokkum, P. G. v., Franx, M., et al. 2012, *ApJS*, 200, 13, doi: [10.1088/0067-0049/200/2/13](https://doi.org/10.1088/0067-0049/200/2/13)
- Bruzual, G., & Charlot, S. 2003, *MNRAS*, 344, 1000, doi: [10.1046/j.1365-8711.2003.06897.x](https://doi.org/10.1046/j.1365-8711.2003.06897.x)
- Calamida, A., Mack, J., Medina, J., et al. 2021, New time-dependent WFC3 UVIS inverse sensitivities, Instrument Science Report WFC3 2021-4, 33 pages
- Calzetti, D., Armus, L., Bohlin, R. C., et al. 2000, *The Astrophysical Journal*, 533, 682, doi: [10.1086/308692](https://doi.org/10.1086/308692)
- Carnall, A. C., McLure, R. J., Dunlop, J. S., et al. 2019, eprint arXiv:1903.11082
- Casertano, S., Mello, D. F. d., Dickinson, M. E., et al. 2000, *AJ*, 120, 2747, doi: [10.1086/316851](https://doi.org/10.1086/316851)
- Dale, D. A., Helou, G., Magdis, G. E., et al. 2014, *ApJ*, 784, 83, doi: [10.1088/0004-637x/784/1/83](https://doi.org/10.1088/0004-637x/784/1/83)
- Dayal, P., Volonteri, M., Schneider, R., et al. 2020, *MNRAS*, 495, 3065, doi: [10.1093/mnras/staa1138](https://doi.org/10.1093/mnras/staa1138)
- Dulude, M. J., Rajan, A., Viana, A., Baggett, S., & Petro, L. 2010, in *Hubble after SM4. Preparing JWST*, 62
- Endsley, R., Stark, D. P., Chevallard, J., & Charlot, S. 2021, *MNRAS*, 500, 5229, doi: [10.1093/mnras/staa3370](https://doi.org/10.1093/mnras/staa3370)
- Fan, X., Carilli, C. L., & Keating, B. 2006, *ARA&A*, 44, 415, doi: [10.1146/annurev.astro.44.051905.092514](https://doi.org/10.1146/annurev.astro.44.051905.092514)
- Finkelstein, S. L., D'Aloisio, A., Paardekooper, J.-P., et al. 2019, *ApJ*, 879, 36, doi: [10.3847/1538-4357/ab1ea8](https://doi.org/10.3847/1538-4357/ab1ea8)
- Fletcher, T. J., Tang, M., Robertson, B. E., et al. 2019, *ApJ*, 878, 87, doi: [10.3847/1538-4357/ab2045](https://doi.org/10.3847/1538-4357/ab2045)
- Flury, S. R., Jaskot, A. E., Ferguson, H. C., et al. 2022, arXiv
- Garilli, B., Guzzo, L., Scodreggio, M., et al. 2014, *Astronomy & Astrophysics*, 562, A23, doi: [10.1051/0004-6361/201322790](https://doi.org/10.1051/0004-6361/201322790)
- Gonzaga, S. 2012, *The DrizzlePac Handbook*, HST Data Handbook. <http://adsabs.harvard.edu/abs/2012drzp.book.....G>
- Griffiths, A., Conselice, C. J., Ferreira, L., et al. 2022, arXiv, doi: [10.48550/arxiv.2211.06162](https://doi.org/10.48550/arxiv.2211.06162)
- Grogin, N. A., Kocevski, D. D., Faber, S. M., et al. 2011, *ApJS*, 197, 35, doi: [10.1088/0067-0049/197/2/35](https://doi.org/10.1088/0067-0049/197/2/35)
- Guaita, L., Talia, M., Pentericci, L., et al. 2017, *Astronomy & Astrophysics*, 606, A19, doi: [10.1051/0004-6361/201730603](https://doi.org/10.1051/0004-6361/201730603)
- Guo, Y., Ferguson, H. C., Giavalisco, M., et al. 2013, *ApJS*, 207, 24, doi: [10.1088/0067-0049/207/2/24](https://doi.org/10.1088/0067-0049/207/2/24)
- Hack, W. J., Cara, M., Sosey, M., et al. 2021, doi: [10.5281/zenodo.5534751](https://doi.org/10.5281/zenodo.5534751)
- Hasinger, G., Capak, P. L., Salvato, M., et al. 2018, *ApJ*, 858, 77, doi: [10.3847/1538-4357/aabacf](https://doi.org/10.3847/1538-4357/aabacf)
- Herenz, E. C., Urrutia, T., Wisotzki, L., et al. 2017, *Astronomy & Astrophysics*, 606, A12, doi: [10.1051/0004-6361/201731055](https://doi.org/10.1051/0004-6361/201731055)
- Hsu, L.-T., Salvato, M., Nandra, K., et al. 2014, *ApJ*, 796, 60, doi: [10.1088/0004-637x/796/1/60](https://doi.org/10.1088/0004-637x/796/1/60)
- Inoue, A. K., Shimizu, I., Iwata, I., & Tanaka, M. 2014, *MNRAS*, 442, 1805, doi: [10.1093/mnras/stu936](https://doi.org/10.1093/mnras/stu936)
- Iwata, I., Inoue, A. K., Matsuda, Y., et al. 2009, *ApJ*, 692, 1287, doi: [10.1088/0004-637x/692/2/1287](https://doi.org/10.1088/0004-637x/692/2/1287)
- Izotov, Y. I., Orlitová, I., Schaerer, D., et al. 2016, *Nature*, 529, 178, doi: [10.1038/nature16456](https://doi.org/10.1038/nature16456)
- Izotov, Y. I., Worseck, G., Schaerer, D., et al. 2021, *Monthly Notices of the Royal Astronomical Society*, 503, 1734, doi: [10.1093/mnras/stab612](https://doi.org/10.1093/mnras/stab612)
- . 2018, *MNRAS*, 478, 4851, doi: [10.1093/mnras/sty1378](https://doi.org/10.1093/mnras/sty1378)

- Jaskot, A. E., & Oey, M. S. 2013, *The Astrophysical Journal*, 766, 91, doi: [10.1088/0004-637x/766/2/91](https://doi.org/10.1088/0004-637x/766/2/91)
- Ji, Z., Giallisco, M., Vanzella, E., et al. 2020, *The Astrophysical Journal*, 888, 109, doi: [10.3847/1538-4357/ab5fdc](https://doi.org/10.3847/1538-4357/ab5fdc)
- Jones, L. H., Barger, A. J., & Cowie, L. L. 2021, *ApJ*, 908, 222, doi: [10.3847/1538-4357/abd5b8](https://doi.org/10.3847/1538-4357/abd5b8)
- Jones, L. H., Barger, A. J., Cowie, L. L., et al. 2018, *ApJ*, 862, 142, doi: [10.3847/1538-4357/aacef8](https://doi.org/10.3847/1538-4357/aacef8)
- Koekemoer, A. M., Faber, S. M., Ferguson, H. C., et al. 2011, *ApJS*, 197, 36, doi: [10.1088/0067-0049/197/2/36](https://doi.org/10.1088/0067-0049/197/2/36)
- Kokorev, V., Brammer, G., Fujimoto, S., et al. 2022, arXiv
- Kriek, M. T., Shapley, A. E., Reddy, N. A., et al. 2015, *ApJS*, 218, 15, doi: [10.1088/0067-0049/218/2/15](https://doi.org/10.1088/0067-0049/218/2/15)
- Kulkarni, G., Keating, L. C., Haehnelt, M. G., et al. 2019, *MNRAS*, 485, L24, doi: [10.1093/mnras/slz025](https://doi.org/10.1093/mnras/slz025)
- Kurk, J., Cimatti, A., Daddi, E., et al. 2013, *Astronomy & Astrophysics*, 549, A63, doi: [10.1051/0004-6361/201117847](https://doi.org/10.1051/0004-6361/201117847)
- Le Fèvre, O., Vettolani, G., Garilli, B., et al. 2005, *A&A*, 439, 845, doi: [10.1051/0004-6361:20041960](https://doi.org/10.1051/0004-6361:20041960)
- Le Fèvre, O., Tasca, L. A. M., Cassata, P., et al. 2015, *A&A*, 576, A79, doi: [10.1051/0004-6361/201423829](https://doi.org/10.1051/0004-6361/201423829)
- Leitherer, C., Ferguson, H. C., Heckman, T. M., & Lowenthal, J. D. 1995, *ApJL*, 454, L19, doi: [10.1086/309760](https://doi.org/10.1086/309760)
- Lilly, S. J., Fèvre, O. L., Renzini, A., et al. 2007, *ApJS*, 172, 70, doi: [10.1086/516589](https://doi.org/10.1086/516589)
- Ma, X., Quataert, E., Wetzel, A. R., et al. 2020, *MNRAS*, 498, 2001, doi: [10.1093/mnras/staa2404](https://doi.org/10.1093/mnras/staa2404)
- Mackenty, J. W., & Smith, L. 2012, CTE White Paper, Tech. Rep., STScI
- Malkan, M. A., Webb, W., & Konopacky, Q. 2003, *ApJ*, 598, 878, doi: [10.1086/379117](https://doi.org/10.1086/379117)
- Marchi, F., Pentericci, L., Guaita, L., et al. 2017, *Astronomy & Astrophysics*, 601, A73, doi: [10.1051/0004-6361/201630054](https://doi.org/10.1051/0004-6361/201630054)
- , 2018, *A&A*, 614, A11, doi: [10.1051/0004-6361/201732133](https://doi.org/10.1051/0004-6361/201732133)
- Masters, D. C., Stern, D. K., Cohen, J. G., et al. 2019, *ApJ*, 877, 81, doi: [10.3847/1538-4357/ab184d](https://doi.org/10.3847/1538-4357/ab184d)
- Momcheva, I. G., Brammer, G. B., Dokkum, P. G. v., et al. 2016, *ApJS*, 225, 27, doi: [10.3847/0067-0049/225/2/27](https://doi.org/10.3847/0067-0049/225/2/27)
- Mostardi, R. E., Shapley, A. E., Nestor, D. B., et al. 2013, *ApJ*, 779, 65, doi: [10.1088/0004-637x/779/1/65](https://doi.org/10.1088/0004-637x/779/1/65)
- Naidu, R. P., Tacchella, S., Mason, C. A., et al. 2020, *ApJ*, 892, 109, doi: [10.3847/1538-4357/ab7cc9](https://doi.org/10.3847/1538-4357/ab7cc9)
- Naidu, R. P., Oesch, P. A., Reddy, N. A., et al. 2017, *ApJ*, 847, 12, doi: [10.3847/1538-4357/aa8863](https://doi.org/10.3847/1538-4357/aa8863)
- Naidu, R. P., Matthee, J., Oesch, P. A., et al. 2021, *Monthly Notices of the Royal Astronomical Society*, 510, 4582, doi: [10.1093/mnras/stab3601](https://doi.org/10.1093/mnras/stab3601)
- Nandra, K., Laird, E. S., Aird, J. A., et al. 2015, *ApJS*, 220, 10, doi: [10.1088/0067-0049/220/1/10](https://doi.org/10.1088/0067-0049/220/1/10)
- Nayyeri, H., Hemmati, S., Mobasher, B., et al. 2017, *ApJS*, 228, 7, doi: [10.3847/1538-4365/228/1/7](https://doi.org/10.3847/1538-4365/228/1/7)
- Nestor, D. B., Shapley, A. E., Kornei, K. A., Steidel, C. C., & Siana, B. D. 2013, *ApJ*, 765, 47, doi: [10.1088/0004-637x/765/1/47](https://doi.org/10.1088/0004-637x/765/1/47)
- Nestor, D. B., Shapley, A. E., Steidel, C. C., & Siana, B. D. 2011, *ApJ*, 736, 18, doi: [10.1088/0004-637x/736/1/18](https://doi.org/10.1088/0004-637x/736/1/18)
- Newman, J. A., Cooper, M. C., Davis, M., et al. 2013, *ApJS*, 208, 5, doi: [10.1088/0067-0049/208/1/5](https://doi.org/10.1088/0067-0049/208/1/5)
- Oesch, P. A., Montes, M., Reddy, N., et al. 2018, *The Astrophysical Journal Supplement Series*, 237, 12, doi: [10.3847/1538-4365/aacb30](https://doi.org/10.3847/1538-4365/aacb30)
- Oke, J. B., & Gunn, J. E. 1983, *Astrophysical Journal*, 266, 713, doi: [10.1086/160817](https://doi.org/10.1086/160817)
- Pahl, A. J., Shapley, A. E., Steidel, C. C., Chen, Y., & Reddy, N. A. 2021, *MNRAS*, 505, 2447, doi: [10.1093/mnras/stab1374](https://doi.org/10.1093/mnras/stab1374)
- Pentericci, L., Garilli, R. J. M. B., Cucciati, O., et al. 2018, *Astronomy & Astrophysics*, 616, A174, doi: [10.1051/0004-6361/201833047](https://doi.org/10.1051/0004-6361/201833047)
- Popesso, P., Dickinson, M., Nonino, M., et al. 2009, *A&A*, 494, 443, doi: [10.1051/0004-6361:200809617](https://doi.org/10.1051/0004-6361:200809617)
- Prichard, L. J., Rafelski, M., Cooke, J., et al. 2022, *The Astrophysical Journal*, 924, 14, doi: [10.3847/1538-4357/ac3004](https://doi.org/10.3847/1538-4357/ac3004)
- Rafelski, M. A., Teplitz, H. I., Gardner, J. P., et al. 2015, *AJ*, 150, 31, doi: [10.1088/0004-6256/150/1/31](https://doi.org/10.1088/0004-6256/150/1/31)
- Reddy, N. A., Steidel, C. C., Erb, D. K., Shapley, A. E., & Pettini, M. 2006, *ApJ*, 653, 1004, doi: [10.1086/508851](https://doi.org/10.1086/508851)
- Redshaw, C., McCabe, T., Otteson, L., et al. 2022, *Research Notes of the American Astronomical Society*, 6, 63, doi: [10.3847/2515-5172/ac6189](https://doi.org/10.3847/2515-5172/ac6189)
- Rivera-Thorsen, T. E., Dahle, H., Chisholm, J., et al. 2019, eprint arXiv:1904.08186
- Robertson, B. E., Ellis, R. S., Furlanetto, S. R., & Dunlop, J. S. 2015, *The Astrophysical Journal Letters*, 802, L19, doi: [10.1088/2041-8205/802/2/119](https://doi.org/10.1088/2041-8205/802/2/119)
- Robertson, B. E., Furlanetto, S. R., Schneider, E. E., et al. 2013, *ApJ*, 768, 71, doi: [10.1088/0004-637x/768/1/71](https://doi.org/10.1088/0004-637x/768/1/71)
- Rutkowski, M. J., Scarlata, C., Henry, A. L., et al. 2017, *ApJ*, 841, L27, doi: [10.3847/2041-8213/aa733b](https://doi.org/10.3847/2041-8213/aa733b)
- Saxena, A., Pentericci, L., Ellis, R. S., et al. 2021
- Shapley, A. E., Steidel, C. C., Strom, A. L., et al. 2016
- Siana, B., Shapley, A. E., Kulas, K. R., et al. 2015, *The Astrophysical Journal*, 804, 17, doi: [10.1088/0004-637x/804/1/17](https://doi.org/10.1088/0004-637x/804/1/17)
- Siana, B. D., Teplitz, H. I., Colbert, J. W., et al. 2007, *ApJ*, 668, 62, doi: [10.1086/521185](https://doi.org/10.1086/521185)
- Siana, B. D., Teplitz, H. I., Ferguson, H. C., et al. 2010, *ApJ*, 723, 241, doi: [10.1088/0004-637x/723/1/241](https://doi.org/10.1088/0004-637x/723/1/241)
- Skelton, R. E., Whitaker, K. E., Momcheva, I. G., et al. 2014, *ApJS*, 214, 24, doi: [10.1088/0067-0049/214/2/24](https://doi.org/10.1088/0067-0049/214/2/24)

- Smith, B. M., Windhorst, R. A., Jansen, R. A., et al. 2018, ApJ, 853, 191, doi: [10.3847/1538-4357/aaa3dc](https://doi.org/10.3847/1538-4357/aaa3dc)
- Smith, B. M., Windhorst, R. A., Cohen, S. H., et al. 2020, ApJ, 897, 41, doi: [10.3847/1538-4357/ab8811](https://doi.org/10.3847/1538-4357/ab8811)
- Smith et al. 2023, in prep., ApJL
- Stark, D. P. 2016, ARA&A, 54, 761 , doi: [10.1146/annurev-astro-081915-023417](https://doi.org/10.1146/annurev-astro-081915-023417)
- Stefanon, M., Labbé, I., Bouwens, R. J., et al. 2017a, eprint arXiv:1706.04613
- Stefanon, M., Yan, H.-J., Mobasher, B., et al. 2017b, ApJS, 229, 32, doi: [10.3847/1538-4365/aa66cb](https://doi.org/10.3847/1538-4365/aa66cb)
- Steidel, C. C., Bogosavljević, M., Shapley, A. E., et al. 2018, ApJ, 869, 123, doi: [10.3847/1538-4357/aaed28](https://doi.org/10.3847/1538-4357/aaed28)
- Steidel, C. C., Pettini, M., & Adelberger, K. L. 2001, The Astrophysical Journal, 546, 665, doi: [10.1086/318323](https://doi.org/10.1086/318323)
- Szalay, A. S., Connolly, A. J., & Szokoly, G. P. 1999, AJ, 117, 68 , doi: [10.1086/300689](https://doi.org/10.1086/300689)
- Szokoly, G. P., Bergeron, J., Hasinger, G., et al. 2004, ApJS, 155, 271 , doi: [10.1086/424707](https://doi.org/10.1086/424707)
- Tang, M., Stark, D. P., Chevallard, J., & Charlot, S. 2019, Monthly Notices of the Royal Astronomical Society, 489, 2572, doi: [10.1093/mnras/stz2236](https://doi.org/10.1093/mnras/stz2236)
- Teplitz, H. I., Rafelski, M. A., Kurczynski, P., et al. 2013, AJ, 146, 159, doi: [10.1088/0004-6256/146/6/159](https://doi.org/10.1088/0004-6256/146/6/159)
- Trump, J. R., Impey, C. D., Elvis, M., et al. 2009, ApJ, 696, 1195 , doi: [10.1088/0004-637x/696/2/1195](https://doi.org/10.1088/0004-637x/696/2/1195)
- Vanzella, E., Cristiani, S., Dickinson, M. E., et al. 2007, A&A, 478, 83 , doi: [10.1051/0004-6361/20078332](https://doi.org/10.1051/0004-6361/20078332)
- Vanzella, E., Giavalisco, M., Inoue, A. K., et al. 2010, The Astrophysical Journal, 725, 1011, doi: [10.1088/0004-637x/725/1/1011](https://doi.org/10.1088/0004-637x/725/1/1011)
- Vanzella, E., Guo, Y., Giavalisco, M., et al. 2012, ApJ, 751, 70, doi: [10.1088/0004-637x/751/1/70](https://doi.org/10.1088/0004-637x/751/1/70)
- Vanzella, E., Balestra, I., Gronke, M., et al. 2016, eprint arXiv:1607.03112, 465, 3803 , doi: [10.1093/mnras/stw2442](https://doi.org/10.1093/mnras/stw2442)
- Vanzella, E., Calura, F., Meneghetti, M., et al. 2018, eprint arXiv:1809.02617
- Vanzella, E., Castellano, M., Bergamini, P., et al. 2022, Astronomy & Astrophysics, 659, A2, doi: [10.1051/0004-6361/202141590](https://doi.org/10.1051/0004-6361/202141590)
- Vasei, K., Siana, B. D., Shapley, A. E., et al. 2016, ApJ, 831, 38, doi: [10.3847/0004-637x/831/1/38](https://doi.org/10.3847/0004-637x/831/1/38)
- Wang, X., Hoag, A. T., Huang, K.-H., et al. 2015, ApJ, 811, 29, doi: [10.1088/0004-637x/811/1/29](https://doi.org/10.1088/0004-637x/811/1/29)
- Wang, X., Teplitz, H., Alavi, A., et al. 2020, in American Astronomical Society Meeting Abstracts, Vol. 235, American Astronomical Society Meeting Abstracts #235, 426.03
- Wang, X., Li, Z., Cai, Z., et al. 2022a, The Astrophysical Journal, 926, 70, doi: [10.3847/1538-4357/ac3974](https://doi.org/10.3847/1538-4357/ac3974)
- Wang, X., Jones, T., Vulcani, B., et al. 2022b, The Astrophysical Journal Letters, 938, L16, doi: [10.3847/2041-8213/ac959e](https://doi.org/10.3847/2041-8213/ac959e)
- Windhorst, R. A., Cohen, S. H., Hathi, N. P., et al. 2011, ApJS, 193, 27, doi: [10.1088/0067-0049/193/2/27](https://doi.org/10.1088/0067-0049/193/2/27)
- Wirth, G. D., Willmer, C. N. A., Amico, P., et al. 2004, AJ, 127, 3121 , doi: [10.1086/420999](https://doi.org/10.1086/420999)
- Wirth, G. D., Trump, J. R., Barro, G., et al. 2015, AJ, 150, 153, doi: [10.1088/0004-6256/150/5/153](https://doi.org/10.1088/0004-6256/150/5/153)
- Xue, Y., Luo, B., Brandt, W. N., et al. 2016, ApJS, 224, 15, doi: [10.3847/0067-0049/224/2/15](https://doi.org/10.3847/0067-0049/224/2/15)
- Yuan, F.-T., Zheng, Z.-Y., Lin, R., Zhu, S., & Rahna, P. T. 2021, The Astrophysical Journal Letters, 923, L28, doi: [10.3847/2041-8213/ac4170](https://doi.org/10.3847/2041-8213/ac4170)